JGR Solid Earth

RESEARCH ARTICLE
10.1029/2023JB027472

Disagreements in Geodetically Inferred Strain Rates in the Western US With Stress Orientations and Geologic Moment Rates

Kaj M. Johnson[1]

[1]Department of Earth and Atmospheric Sciences, Indiana University, Bloomington, IN, USA

Key Points:

- I implement an elasticity-based inversion of geodetic data for strain rate
- Systemic differences in orientation of stress and strain rate in Cascadia, San Andreas Fault, and eastern Basin-Range
- The total geodetic moment rates are higher than geologic moment rates within most regions of the western US

Correspondence to:
K. M. Johnson,
kajjohns@indiana.edu

Citation:
Johnson, K. M. (2024). Disagreements in geodetically inferred strain rates in the western US with stress orientations and geologic moment rates. *Journal of Geophysical Research: Solid Earth*, *129*, e2023JB027472. https://doi.org/10.1029/2023JB027472

Received 20 JULY 2023
Accepted 27 MAR 2024

Author Contribution:
Conceptualization: Kaj M. Johnson
Funding acquisition: Kaj M. Johnson
Methodology: Kaj M. Johnson
Software: Kaj M. Johnson
Writing – original draft: Kaj M. Johnson
Writing – review & editing: Kaj M. Johnson

Abstract I employ an elasticity-based method to invert a geodetically derived surface velocity field in the western US using for present-day surface strain rate fields with uncertainties. The method uses distributed body forces in a thin elastic sheet and allows for discontinuities in velocity across creeping faults using the solution for dislocations in a thin elastic plate. I compare the strain rate fields with previously published stress orientations and moment rates from geological slip rate data and previous geodetic studies. Geologic and geodetic moment rates are calculated using slip rate and off-fault strain rates from the 2023 US National Seismic Hazard Model (NSHM) deformation models. I find that computed total geodetic moment rates are higher than NSHM summed moment rates on faults for all regions of the western US except the highest deforming rate regions including the Western Transverse Ranges and the northern and southern San Andreas Fault (SAF) system in California. Computed geodetic moment rates are comparable to the moment rates derived from the geodetically based NSHM deformation models in all regions. I find systematic differences in orientations of maximum horizontal shortening rate and maximum horizontal compressive stress in the Pacific Northwest region and along much of the SAF system. In the Pacific Northwest, the maximum horizontal stress orientations are rotated counterclockwise 40–90° relative to the maximum horizontal strain rate directions. Along the SAF system, the maximum horizontal stresses are rotated systematically 25–40° clockwise (closer to fault normal) relative to the strain rates.

Plain Language Summary Geodetic measurements of surface velocities can be converted to strain rate which is a measure of the distortion rate of the crust. Strain rate is an important quantity for earthquake studies because it can be related to the rate of elastic stored energy (called moment) available for future earthquakes. In this paper I employ a new method to invert the surface velocity field in the western US for present-day surface strain rates. I convert the strain rates to crustal moment rates and compare this with moment release rates computed from previous estimates of fault slip rates from geology as well as with model moment rates from the 2023 US National Seismic Hazard Model (NSHM). I find that computed total geodetic moment rates are higher than NSHM model moment rates on faults for many regions of the western US. I also find systematic differences in present-day strain rates and total stress in the crust indicating that the total stress in the crust is not simply the accrual of present-day deformation.

1. Introduction

One of the long-term goals of establishing geodetic networks in deforming plate boundary settings is to use measurements of ground motions during interseismic periods to infer earthquake potential from measurements of strain accumulation. Geodetic data such as Global Navigation Satellite Systems (GNSS) have often been used to estimate present-day moment rates by computing surface strain rates from GNSS derived velocities and integrating them to obtain Kostrov-type moment deficit rate (Savage & Simpson, 1997). GNSS data are also used to estimate slip rates on crustal faults through the use of various types of kinematic models and the assumption that strain rate can be related slip deficit rates, modeled as back-slip, on faults (e.g., Harris & Segall, 1987; McCaffrey, 2005; Meade et al., 2002; Savage & Burford, 1973; Savage, 1983). The first approach benefits from making no assumptions about faults; the estimated moment rate is derived directly from strain rate observations. The second approach uses the additional information from the geometry of faults to obtain slip rates on those faults. When this is done, some fraction of the strain rate field may remain unaccounted-for, for example, due to small-scale faulting, folding, pressure dissolution, and other similar deformation mechanisms that occur off of major faults (e.g., Gray et al., 2017; Herbert et al., 2013). Some of these strain mechanisms are inelastic and

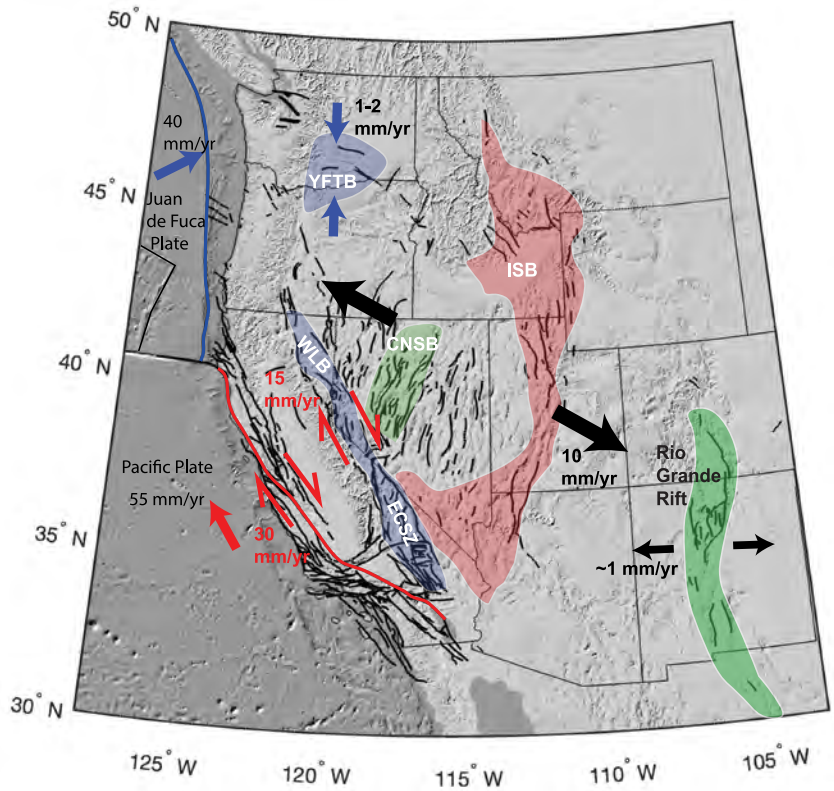

Figure 1. Western US tectonic setting and major deformation belts. San Andreas Fault shown with heavy red line. Cascadia subduction zone trench shown with heavy blue line. Red opposing lateral arrows indicated approximate right lateral shear rates. Black divergent arrows indicate the ~ 10 mm/yr of extension across the northern Basin and Range region. Blue convergent arrows show 1–2 mm/yr shortening rate across the Yakima Fold and Thrust Belt (YFTB). IWSB = Intermountain Seismic Belt. Heavy black lines are fault traces from 2014 US National Seismic Hazard Model (Petersen et al., 2014). CNSB = Central Nevada Seismic Belt. WLB = Walker Lane Belt. ECSZ = Eastern California Shear Zone. WTR = Western Transverse Ranges.

permanent in nature, and thus do not contribute to earthquake hazard, but may contribute to the overall strain rate field measured geodetically. Quantifying these different components of the strain rate field (on-vs. off-fault, elastic vs. inelastic) is critical for accurately integrating geodetic data and inversions into seismic hazard models. It is also critical to accurately quantify uncertainty in the estimated strain rate itself, due to formal data errors, sparse and uneven data coverage, and interpolation errors, among other sources.

Geodetically derived on-fault and off-fault deformation was examined systematically in the western US for the 2023 update to the National Seismic Hazard Model (NSHM 2023; Pollitz et al., 2022). These studies used the GNSS derived velocity field and geologic slip rate constraints with various kinematic deformation models to infer fault slip rates and off-fault strain rates. The western US is a diffuse and tectonically-complicated deformation zone that accommodates relative motion between the Pacific or Juan de Fuca plate and North America (Figure 1). The NSHM 2023 model includes 1017 active faults that are known to accommodate much of the distributed deformation across the western US. Broadly, the San Andreas fault (SAF) (heavy red lines in Figure 1) and neighboring faults accommodated roughly 30 mm/yr of the approximately 55 mm/yr of relative Pacific-North America plate motion. About 15 mm/yr of this motion is accommodated across zones of faults in the Eastern California Shear Zone (ECSZ) and Walker Lane Belt (WLB). About 10 mm/yr of present-day opening across the basin and range region is accommodated largely by faults within the seismically active Central Nevada Seismic Belt (CNSB) and Intermountain Seismic Belt (ISB). The Rio Grande Rift accommodates about 1 mm/yr of extension on the eastern side of the Colorado Plateau. Relative motion between the subducting Juan de Fuca Plate and North America is accommodated at the Cascadia subduction zone in the Pacific Northwest.

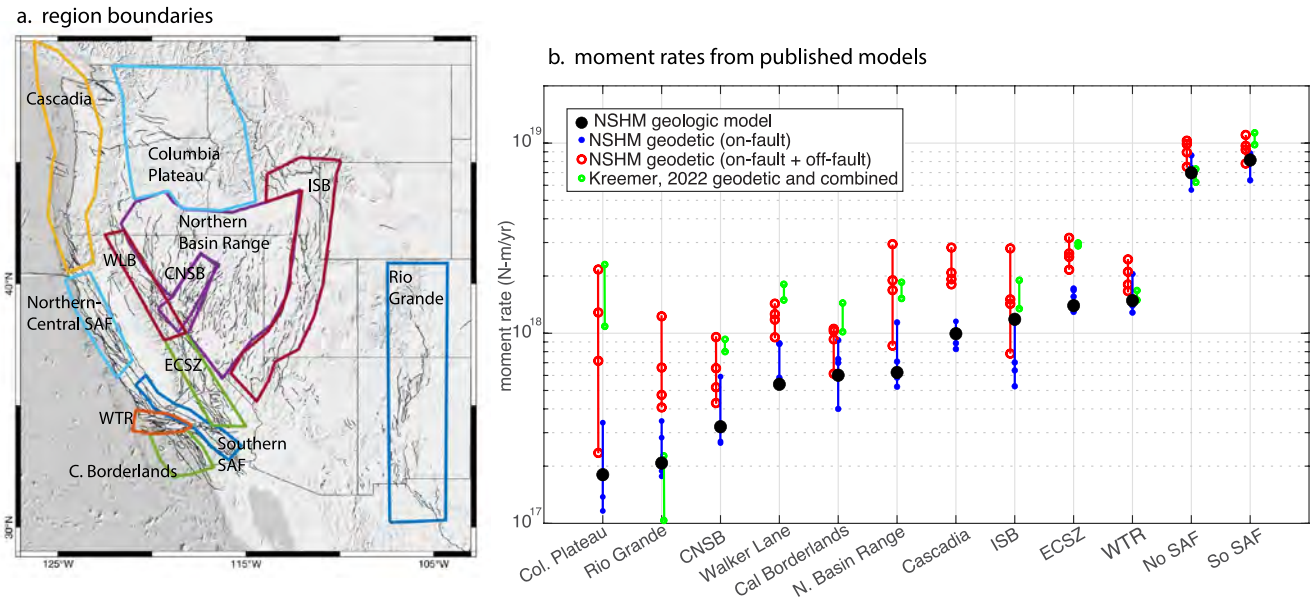

Figure 2. Summary of moment rates in the 2023 National Seismic Hazard Model (NSHM) deformation models and Kreemer and Young (2022). (a) Region boundaries used to compute moments. (b) Summed moments in the regions shown in panel (a). Moments from four geodetically-based NSHM models are shown with four blue filled circles connected with a blue line (on-fault strain rates) and four red open circles connected with a red line (on-fault + off-fault strain rates). Moment rates from the NSHM 2023 geologic deformation model, which is based largely on geologic slip rate data, shown with black circles. Moment rates from Kreemer and Young (2022) strain rates are computed using Savage and Simpson (1997). Green dots show moments from Kreemer's geodetic-only and combined geodetic and geologic models. On-fault moment rates from NSHM 2023 models are computed using model slip rates and upper and lower rupture depths provided by the NSHM 2023 model.

A finding from the suite of kinematic deformation models designed for NSHM 2023 model, as summarized by Pollitz et al. (2022), is that 30%–60% of the total moment rate in the geodetic deformation models is attributed to off-fault deformation distributed through the crust, while the total on-fault moment rate in the geodetic models is similar to the on-fault moment rate inferred from the geologic deformation model that relies primarily on geologic observations. Figure 2 shows a summary of the NSHM 2023 deformation model moment rates by region (note the Cascadia region does not include the contribution from the subduction interface). The range in geodetically-based model on-fault moment rates (small blue circles) contains the geologic model rate in all regions suggesting good agreement between the geodetic and geologic model estimates. The range of total moment rates by region in the geodetically-based models (red circles), which is computed from fault slip rates and off-fault strain rates in each region, is systematically higher than the geologic model rate (the geologic model does not include off-fault deformation). However, there is quite a lot of scatter in the total moment rates in many of the regions, and the spatial distributions of off-fault moment rates differ substantially across the four geodetically-based NSHM 2023 deformation models (see Pollitz et al., 2022) indicating that the inferred off-fault moment rate is quite model-dependent. It is unclear from the NSHM models what portion of the large off-fault deformation is truly required by geodetic data and what portion might be simply attributed model deficiencies or noisy data. It is also unclear the extent to which the geologic deformation models might be missing moment on unmodeled faults. The study of Kreemer and Young (2022) provides a hint that geodetic data does indeed require higher total moment rates than implied by the on-fault NSHM 2023 rates. Moment rates from the geodetic-only and the combined geodetic and geological strain rate maps of Kreemer and Young (2022) are shown in Figure 2b. The NSHM 2023 and Kreemer moment rates have been computed in the same way; horizontal strain rate components are converted to moment using the formula of Savage and Simpson (1997) and assuming a 15 km seismogenic depth. In nearly all regions, the Kreemer moment rates are higher than the NSHM on-fault rates and are a broadly comparable to the total on-fault plus off-fault NSHM geodetic rates. Ward (1998) also used the Savage and Simpson (1997) formula to compare geodetic moment rates with seismic moment rate from historical seismicity and moment rates from geologic slip rate studies. Ward (1998) found geodetic moment rates were 20% higher than geologic rates in California, and both seismic and geodetic moment rates greatly exceed geologic rates in the Basin an Range. However, spatial coverage of geodetic data in the late 1990s was far inferior to the spatial coverage available today.

One purpose of this study is to explore the relationship between inferred long-term geologic moment release rates on faults in the western US with present-day moment accumulation rates inferred from geodesy. I will examine the geodetic moment rate problem described above by computing the spatial distribution and uncertainties in geodetically-inferred moment rates directly from strain rates and comparing with geologic moment release rates on faults. I will also compare horizontal principal strain rate orientations with previously published maximum horizontal stress orientations. Stress orientations provide an independent measure of the state of deformation in the crust and are sometimes used as constraints on deformation models (e.g., Bird, 2009; Flesch et al., 2007; Shen & Bird, 2022). However, there are notable cases where principal strain rate and stress orientations are inconsistent (e.g., Townend & Zoback, 2006; Wang, 2000), indicating a difference in the state of total stress in the crust and the instantaneous rate of deformation.

2. Strain Rate Method

Previous approaches to compute strain rates have used baselines (e.g., Savage, 1983; Ward, 1994) or spatial interpolation onto a regular grid and application of numerical derivatives. Interpolation approaches provide a means of downscaling GNSS observations, but data noise and uneven station spacing means that any interpolation scheme involves some degree of data misfit and, in addition, some method is required for regularizing the basis coefficients to obtain a smooth field. Depending on the method, this can be accomplished by minimizing the number of spatial wavelengths retained in the fitting function or the degree of smoothness of the solution.

A variety of interpolation methods have been adopted for computing strain rates. Some interpolation approaches fit the velocity field using basis functions (polynomials, splines, wavelets, etc.) (e.g., Beavan & Haines, 2001; Feigl et al., 1993; Hackl et al., 2009; Haines & Holt, 1993; Tape et al., 2009). A few approaches use elasticity theory (e.g., Haines et al., 2015; Noda & Matsu'ura, 2010; Sandwell & Wessel, 2016). Weighted mean approaches, which include methods based on an estimated spatial covariance functions, have been also been adopted (e.g., El-Fiky & Kato, 1998; Goudarzi et al., 2015; Shen et al., 1996, 2015). Kreemer et al. (2018) developed the robust Median Estimation of Local Deformation (MELD) algorithm method that computes a weighted median of a series of least-squares estimates that account for variable station spacing. Pagani et al. (2021) regularized strain rate inversions of irregularly spaced data using a trans-dimensional Bayesian method that accounts for uncertainty due to variable grid spacing.

A few geodetically-based strain rate models have been published for either the entire western US or sub regions. The global strain rate model of Kreemer et al. (2014) includes the western US and provides strain rate calculations at a spacing of ∼25 km. A strain rate map was created for the 2018 US National Seismic Hazard Map project (Petersen et al., 2014). Bomberger et al. (2018) computed strain rates in the western US and examined correlations with topography. Other strain rate maps have been created for sub regions of the western US (e.g., Tape et al., 2009; Zeng et al., 2018). Pagani et al. (2021) and Hackl et al. (2009) computed strain rates from geodetic data in the southwest Unite States. Most recently, Kreemer and Young (2022) computed a suite of strain rate models for the western US constrained by geologic and geodetic data using a combination of the MELD algorithm Kreemer et al. (2018) and the method of Haines and Holt (1993).

For this study, I develop an elasticity-based strain rate inversion method that is based on the Vertical Derivatives of Horizontal Stress (VDoHS) method of Haines et al. (2015) and the gpsgridder method (implemented in GMT) by Sandwell and Wessel (2016). The VDoHS method computes velocity and strain rate fields using a finite element solution for body forces in a thin elastic plate. The method inverts surface velocity observations for the spatial distribution vertical derivatives of horizontal stresses (equivalent body forces). Sandwell and Wessel (2016) developed a method similar to the VDoHS method to compute a smoothed velocity field from scattered data. They derive the analytical Green's functions for a point body force in a thin elastic sheet (flat sheet) and use them to calculate displacements directly instead of solving a finite element problem. The analytical solution method has been implemented as an interpolation algorithm of 2-D vector data as a module called gpsgridder in the Generic Mapping Tools (Wessel et al., 2013). The relationship between displacements and body force magnitude is linear and depends on one elastic parameter, Poisson's ratio. The Sandwell and Wessel (2016) method works by placing 2N body forces at N geodetic observation coordinates (two orthogonal force vectors). Each observation coordinate has an east and north velocity/displacement component, so there are 2N observations and 2N unknowns, providing a unique solution for body forces and a unique interpolation solution.

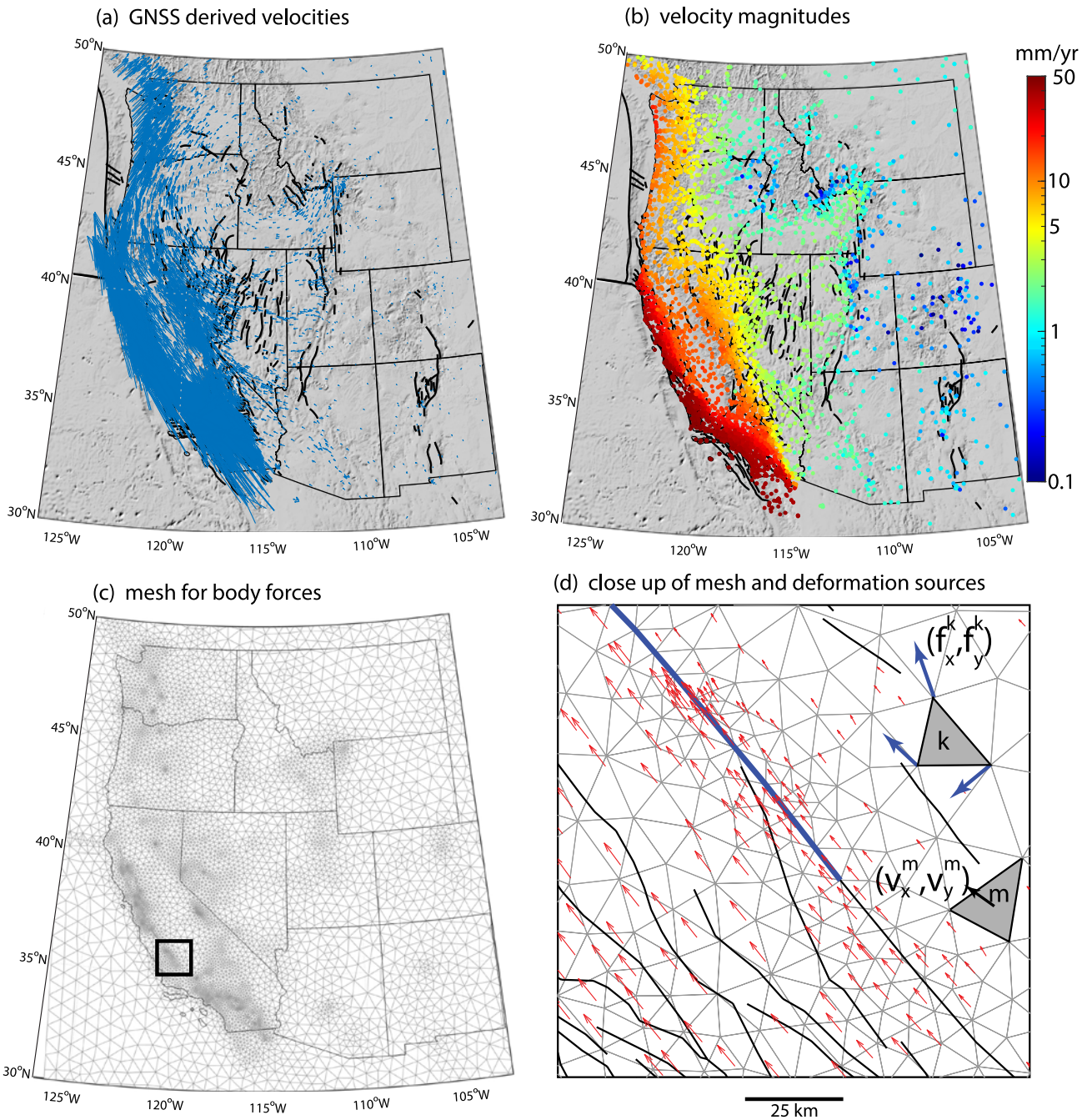

Figure 3. (a) Global Navigation Satellite Systems (GNSS) derived velocity field of Zeng (2022). Fault traces from 2014 US National Seismic Hazard Model (Petersen et al., 2014). (b) Magnitude of GNSS-derived velocities in log color scale. (c) Triangular mesh used to estimate velocity and strain rate fields. Node spacing is proportional to GNSS data spacing. (d) Close-up of triangular mesh and GNSS velocity field. Location is shown with block box in panel (c). Gray shaded triangles illustrate computed velocities (V_x, V_y) at mth triangle centroid due to body forces (f_x,f_y) at nodes of kth triangle. Heavy blue fault trace indicates section of San Andreas Fault modeled as creeping using dislocations in a thin elastic sheet.

In my method, I adopt the analytical thin-elastic-sheet Green's functions presented in Sandwell and Wessel (2016), but I set up the velocity field interpolation as an over-determined inverse problem, similar to the VDoHS method (Haines et al., 2015). As illustrated in Figure 3c, I discretize the western US into triangular elements using MESH2D, a Delaunay-based unstructured mesh generator implemented in Matlab (Engwirda, 2014). The spacing of nodes is scaled with the spacing of velocity observation points (Zeng, 2022) such that the mesh is more dense in areas with more data. I place body forces at the node points and solve for velocity

and strain rate at the centroids of the triangles, as illustrated in Figure 3d. Although not shown in Figure 3, I also include velocity pseudo-observations at the centers of off-shore triangles on the Pacific and Juan de Fuca plates to impose relative motions between those plates and North America. The velocities at those off-shore triangles are computed using MORVEL rotation rate Euler poles (DeMets et al., 2010).

I must also account for discontinuities in the velocity field across faults that creep at the surface. A number of faults in California are known to display substantial surface creep. A surface creep rate data set for California was compiled for the Unified California Earthquake Rupture Forecast, version 3 (UCERF3) (Field et al., 2014) as well as a surface creep rate model that assigned creep rates to fault sections in the model. In this study, I use the surface creep rate model from UCERF3 to constrain the velocity discontinuity across creeping faults.

An open-source version of the code, BforStrain, that implements the method described in this manuscript is available as a public GitHub repository (Johnson, 2023b).

2.1. Basic Method: No Strain Rate Minimization

I first describe the basic method in this section and then I describe a two-step procedure in which I minimize strain rates in low deforming rate regions. The mesh is generated with traces of creeping faults (blue lines in Figure 3d) embedded as edges such that the sides of triangles align with the faults. I model surface creep rate with 2D dislocations in a thin elastic plate along the creeping fault traces. Let $\mathbf{G}_c$ be a matrix of Green's functions that relate unit slip rate on the 2D dislocations to velocities in the sheet, let $\mathbf{s}_c$ be a vector of model creep rates on the faults, and let $\mathbf{c}$ be the vector of observed surface creep rates from the UCERF3 model. Also, let $\mathbf{G}_v$ be the matrix of body force Green's functions given by Sandwell and Wessel (2016), let $\mathbf{f}$ be a vector of body forces in the elastic sheet, and let $\mathbf{v}$ be the vector of observed surface velocities. The surface velocities are related to the model parameters as,

$$\mathbf{v} = \mathbf{G}_v \mathbf{f} + \mathbf{G}_c \mathbf{s_c}. \tag{1}$$

Similarly, the body force solution of Sandwell and Wessel (2016) is used to construct a matrix of Green's functions, $\mathbf{G}_\epsilon$, relating strain rates at centroids of triangles to body forces, and the 2D dislocation solution provides a matrix of Green's functions, $\mathbf{G}_{c,\epsilon}$, relating creep on faults to surface strain rates as,

$$\epsilon = \mathbf{G}_\epsilon \mathbf{f} + \mathbf{G}_{c,\epsilon} \mathbf{s_c}. \tag{2}$$

Given the GNSS derived surface velocities, $\mathbf{v}_{obs}$, I seek to solve the observation equation,

$$\mathbf{v}_{obs} = \mathbf{G}_v \mathbf{f} + \mathbf{G}_c \mathbf{s_c} + \varepsilon, \tag{3}$$

for the distribution of body forces and surface creep rates that "best fits" the data where ε is Gaussian-distributed noise. Equation 3 is a highly under-determined system of equations, so I add an additional damping constraint on the magnitude of body forces and also constrain the surface creep rates to be similar to the UCERF3 creep rates, $\mathbf{c}$, by solving the following weighted system of equations,

$$\begin{bmatrix} \Sigma_v^{-1/2}\mathbf{v}_{obs} \\ \beta\mathbf{c} \\ \mathbf{0} \end{bmatrix} = \begin{bmatrix} \Sigma_v^{-1/2}\mathbf{G}_v & \Sigma_v^{-1/2}\mathbf{G}_c \\ \mathbf{0} & \beta\mathbf{I} \\ \alpha\mathbf{I} & \mathbf{0} \end{bmatrix} \begin{bmatrix} \mathbf{f} \\ \mathbf{s_c} \end{bmatrix}, \tag{4}$$

where Σ_v is the velocity data covariance matrix (diagonal in this study), α is the damping parameter that determines the relative weight placed on fitting the velocity data versus keeping the body forces small, and β determines the relative weight placed on matching surface creep rates to the UCERF3 creep rate model. To simplify notation, I combine the two vectors of unknowns and first two rows of Equation 4, and write the system as,

$$\begin{bmatrix} \mathbf{d_w} \\ \mathbf{0} \end{bmatrix} = \begin{bmatrix} \mathbf{G}_w \\ \alpha\mathbf{L} \end{bmatrix} \mathbf{m}, \tag{5}$$

where $\mathbf{L} = \begin{bmatrix}\mathbf{I} & \mathbf{0}\end{bmatrix}$ and $\mathbf{m} = \begin{bmatrix}\mathbf{f} & \mathbf{s_c}\end{bmatrix}^T$ is a vector of unknown body forces and fault creep rates. This is a standard linear system that can be solved with a least squares formula. The generalized inverse is

$$\mathbf{G}^\sharp = \left[\mathbf{G}_w^T\mathbf{G}_w + \alpha^2\mathbf{L}^T\mathbf{L}\right]^{-1}\mathbf{G}_w^T, \tag{6}$$

and the best-fitting body forces and creep rates, for a given α are

$$\mathbf{m}_\alpha = \begin{bmatrix}\mathbf{f}_\alpha \\ \mathbf{s_c}_\alpha\end{bmatrix} = \mathbf{G}^\sharp\mathbf{d_w}, \tag{7}$$

with covariance matrix,

$$\Sigma_\alpha = \mathbf{G}^\sharp\left(\mathbf{G}^\sharp\right)^T. \tag{8}$$

From this least squares solution I can write the predicted strain rates due to best-fitting body forces and creep rates as,

$$\epsilon_\alpha = \mathbf{G}_\epsilon\,\mathbf{f}_\alpha + \mathbf{G}_{c,\epsilon}\mathbf{s_c}_\alpha. \tag{9}$$

Then, linear error propagation provides the full covariance matrix for unknown strain rate components and creep rates for a given smoothing parameter, α,

$$\Sigma_{\epsilon,\alpha} = \begin{bmatrix}\mathbf{G}_\epsilon & \mathbf{G}_{c,\epsilon}\end{bmatrix}\Sigma_\alpha\begin{bmatrix}\mathbf{G}_\epsilon & \mathbf{G}_{c,\epsilon}\end{bmatrix}^T. \tag{10}$$

The posterior probability of strain rate given data, $\mathbf{d}$, and smoothing parameter, α is a Gaussian distribution,

$$p(\epsilon|\mathbf{d},\alpha) = (2\pi)^{-k/2}|\Sigma_{\epsilon,\alpha}|^{-1/2}\exp\left\{-0.5(\epsilon-\epsilon_\alpha)^T\Sigma_{\epsilon,\alpha}^{-1}(\epsilon-\epsilon_\alpha)\right\}. \tag{11}$$

where k is the length of vector ϵ. To account for the unknown smoothing parameter, α, I want to integrate over a range of values for α. I can write the joint distribution for strain rate, ϵ, and α given the data with the identity,

$$p(\epsilon,\alpha|\mathbf{d}) = p(\epsilon|\alpha,\mathbf{d})p(\alpha|\mathbf{d}), \tag{12}$$

where the first distribution on the right side is given by Equation 11 and the second distribution is the posterior distribution of α given data. The posterior distribution of strain rate for all values of α is obtained by marginalizing Equation 12 over α,

$$p(\epsilon|\mathbf{d}) = \int_{-\infty}^{\infty} p(\epsilon|\alpha,\mathbf{d})p(\alpha|\mathbf{d})d\alpha. \tag{13}$$

Various methods have been adopted for these types of inversions to select smoothing parameter, α, including subjective methods such as trade-off curves and objective means such as Akaike's Bayesian information criterion. Fukuda and Johnson (2010) presented a Monte Carlo method for estimating $p(\epsilon|d)$ for similar damped least squares inversion problems. Here, I take a simpler, but more subjective, approach and assume that all α values within a range are equally likely, that is, $p(\alpha|\mathbf{d})$ is taken as a uniform distribution over an interval. I identify the range of equally likely α values by conducting a series of damped inversions (Equations 5–9) for a wide range of α values. The posterior distribution, $p(\epsilon|d)$ is approximated with discrete samples drawn from the posterior distributions (Equation 10) for each α value. For each of fifteen α values, I generate 100 realizations of $p(\epsilon|d, \alpha)$ by drawing random samples using Equation 10. These 1,500 samples taken together represent discrete samples (or realizations) of the posterior distribution p $(\epsilon|d)$.

2.2. Strain Rate Minimization Step

For some inversions, I add an additional step to directly minimize the strain rate components in areas of low strain rate. I first solve the inversion in the previous section. Then, I identify cells with total strain rate, measured as $\sqrt{\epsilon_{11}^2 + \epsilon_{12}^2 + \epsilon_{22}^2}$, below a specified threshold strain rate. Within these cells I further constrain the strain rate components to be near zero. Let $\mathbf{G}_{\epsilon}^{i}$ and $\mathbf{G}_{c,\epsilon}^{i}$ be the matrices of strain rate Greens functions for body forces and fault creep, respectively, in the i rows corresponding with cells with total strain rate below the threshold. I now solve,

$$\begin{bmatrix} \Sigma_v^{-1/2}\mathbf{v}_{obs} \\ \beta\mathbf{c} \\ \mathbf{0} \\ \mathbf{0} \end{bmatrix} = \begin{bmatrix} \Sigma_v^{-1/2}\mathbf{G}_v & \Sigma_v^{-1/2}\mathbf{G}_c \\ \mathbf{0} & \beta\mathbf{I} \\ \alpha\mathbf{I} & \mathbf{0} \\ \gamma\mathbf{G}_{\epsilon}^{i} & \gamma\mathbf{G}_{c,\epsilon}^{i} \end{bmatrix} \begin{bmatrix} \mathbf{f} \\ \mathbf{s_c} \end{bmatrix}, \tag{14}$$

where γ is another subjective parameter that determines the relative weight of minimizing strain rate components versus satisfying all other constraints. The generalized inverse for this problem is,

$$\mathbf{G}^{\sharp} = \left[\mathbf{G}_w^T\mathbf{G}_w + \alpha^2\mathbf{L}^T\mathbf{L} + \gamma^2\mathbf{G}_i^T\mathbf{G}_i\right]^{-1}\mathbf{G}_w^T, \tag{15}$$

where $\mathbf{G}_i$ contains the bottom row of matrices in Equation 14. The strain rates and uncertainties are computed in the same way as before using Equations 7–13.

For the inversion results in this paper, I have hand-tuned the parameters β and γ by trial-and-error. A value of $\beta = 1$ is selected so that the surface creep rates are reasonably fit by the model, and $\gamma = 400$ is identified as a value that reduces moment rates in low deformation regions (for strain rates less than 0.005 micro-strain per year) without significantly degrading the fit to the velocity data.

3. Results

For this study I present the results from both a "smooth" and "rough" inversion. For the smooth inversion I select α values that correspond with reduced χ^2 ranging from 3 to 5, meaning the GNSS derived velocities are fit, on average to within three to five times the formal variances in data error. For the rough inversion I select a range of α values corresponding with reduced χ^2 ranging from 1 to 2. This allows us to compare results that fit the geodetic data well and smoother models that do not fit as well. I also produce two-step strain rate minimization versions of the smooth and rough models for a total of four strain rate models. All computed realizations of strain rate and velocity components are publicly available in a Zenodo repository (Johnson, 2023a).

3.1. Velocity Field

The mean velocity field is shown in Figure 4 for the rough inversion without minimization. The velocity magnitudes are shown with various color scales in Figure 4 to accentuate velocity gradients across the major deformation belts labeled in Figure 1. The velocity gradients across the SAF system and the Cascadia subduction zone are evident in Figure 4a. The velocity gradient across the ECSZ and WLB are evident in Figure 4b, and across the ISB in Figure 4c. Seven velocity profiles across different regions of the western US are shown in Figure 5 for the same rough inversion without minimization. The velocity profiles show the GNSS derived observations and the mean and range of the estimated velocities. Shallow fault creep occurs largely in northern and central California and is evident as jumps in velocity profile 1 (San Andreas), profile 3 (Hayward Fault) and profile 5 (Maacama and Bartlett Springs Faults).

3.2. Strain Rates

In the next section I summarize broad results for the entire western US and in the section after that I look in detail at strain rate results in various regions.

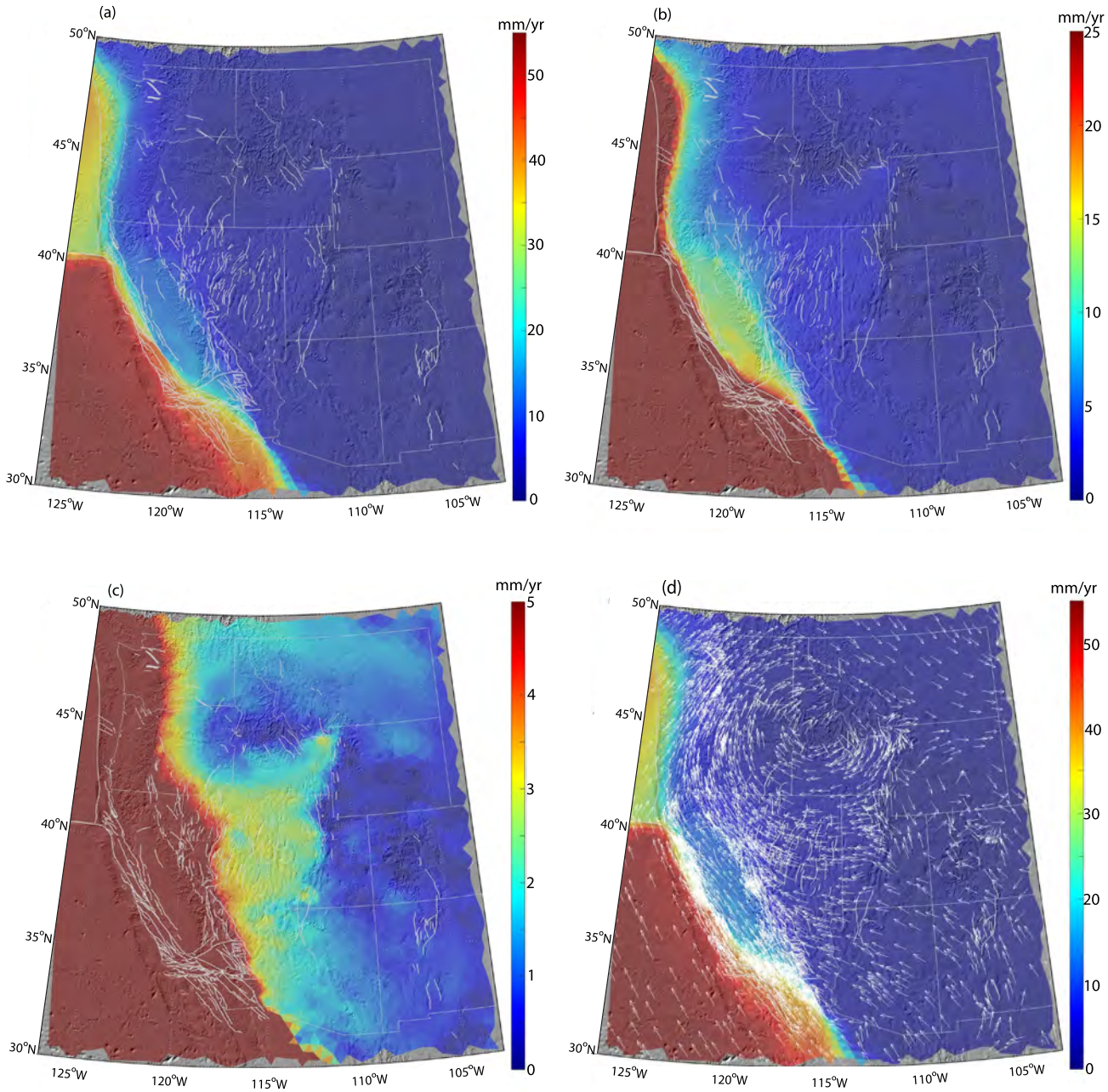

Figure 4. Mean velocity field for rough inversion without minimization step. Color shows magnitude of velocity. (a) Velocity field without color saturation. (b) Velocity field with color saturation at 25 mm/yr to highlight gradients across the Eastern California Shear Zone and Walker Lane Belt. (c) Velocity field with color saturation at 10 mm/yr to highlight gradients across the northern Basin and Range. (d) Vectors show velocity field directions (vectors are all equal length).

3.2.1. Overview of Entire Western United States

The four strain rate results for the entire western US are summarized in Figures 6–11. The maximum shear strain rates and dilatation rates are shown in Figures 6 and 7 for all four inversions. Strain rates are shown only for cells that contain at least one strain rate component that is different from zero at the 2-standard-deviation level for the smooth inversions and 1-standard-deviations for the rough models. Broadly, the spatial distributions of maximum shear strain rate and dilatation are similar to previously published strain rate maps (e.g., Kreemer & Young, 2022; Zeng et al., 2018). Highest shear strain rates are associated with the Cascadia subduction zone, the SAF system, the Eastern California - Walker Lane Shear belts and the ISB.

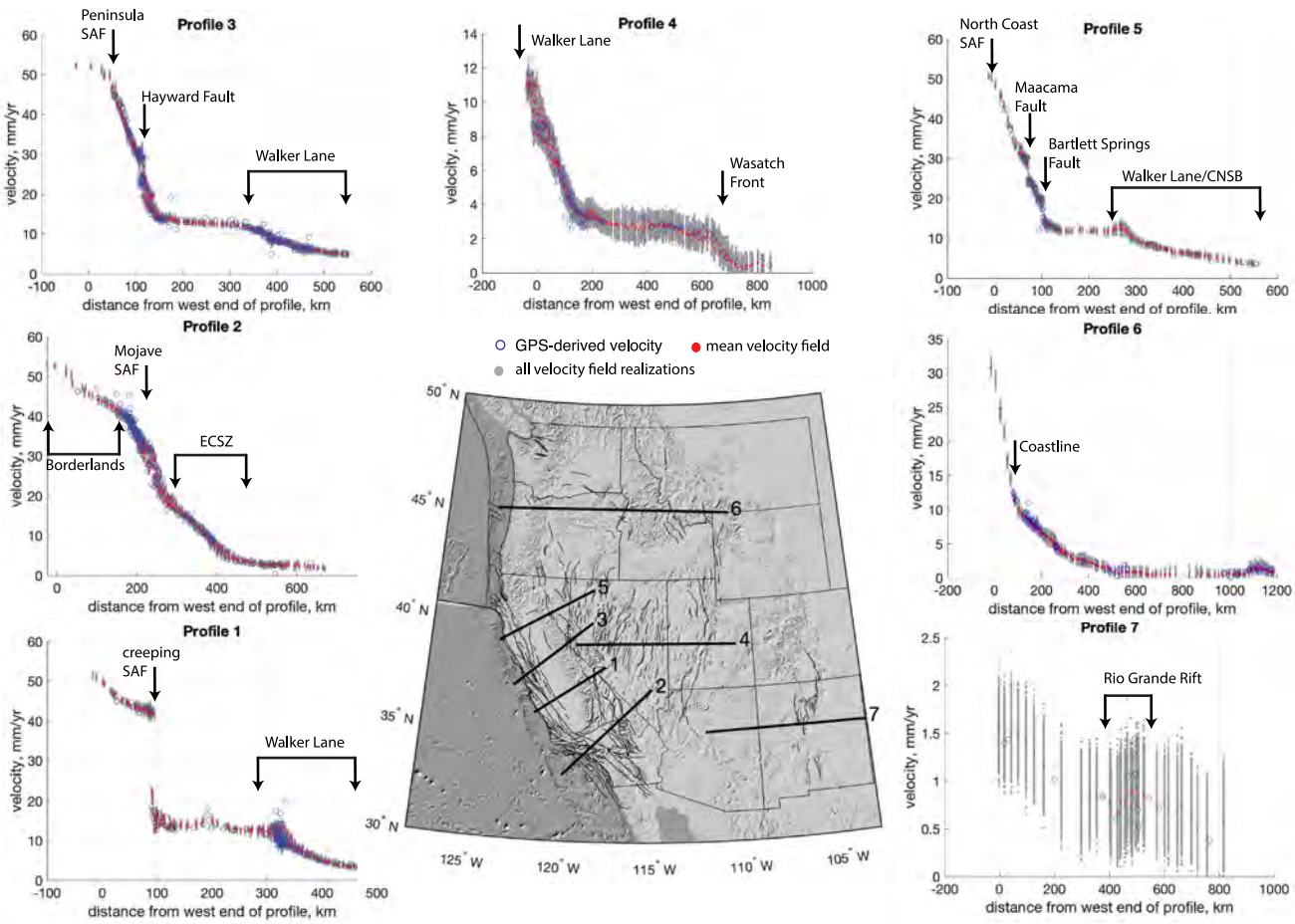

Figure 5. Velocity field profiles for rough inversion without minimization step. Velocities within 20 km of each profile line are projected onto profiles. Global Navigation Satellite Systems derived velocities shown with blue circles. Mean estimated velocity field shown with red filled circles. All realizations are shown with gray filled circles.

In this study, I am particularly interested in the uncertainties in strain rates, especially in low rate regions where there tends to be disagreement between geologic and geodetic moment rates (Figure 2). The "smooth" inversions fit the geodetic data with reduced χ^2 ranging from 3 to 5 with relatively small uncertainties, whereas the "rough" inversions fit data with reduced χ^2 ranging from 1 to 2 with relatively large uncertainties. Figure 8 shows the uncertainties on orientations of the principal strain rates and the coefficient of variation (COV) (mean divided by standard deviation) of maximum shear strain rates for both inversions without the minimization step. Principal strain rate directions and 95% confidence regions are shown in Figures 8a and 8b. The 2-standard deviation confidence intervals are shown with uncertainty wedges for the larger of the two principal strain rate components and the mean of the smaller component is shown with a line. Blue color indicates shortening and red color indicates extension. As expected, uncertainties of the principal strain rate directions are smaller in the smooth model and there is considerably more spatial heterogeneity in principal directions in the rough model. The spatial patterns of principal directions are similar in the smooth and rough models at wavelengths of several hundred km, but there are disagreements in direction and even sign of the principal values at shorter wavelengths. In the smooth model the maximum shear strain rates exceed the standard deviation (COV>1) everywhere except some small pockets within low deformation rate regions. However, in the rough model the maximum shear strain rates are much more uncertain with maximum shear strain rate at or below the standard deviation over large areas of the western US.

Strain rate "style" is shown in Figure 9 for both inversions without the minimization step. Here, strain rate style is computed as a ratio of principal strain rates, $-(\epsilon_1 + \epsilon_2)/(|\epsilon_1| + |\epsilon_2|)$, and ranges from -1 (normal faulting style) to $+1$ (reverse faulting style), with strike-slip faulting style at zero. As in Figure 6, strain rate style values are shown

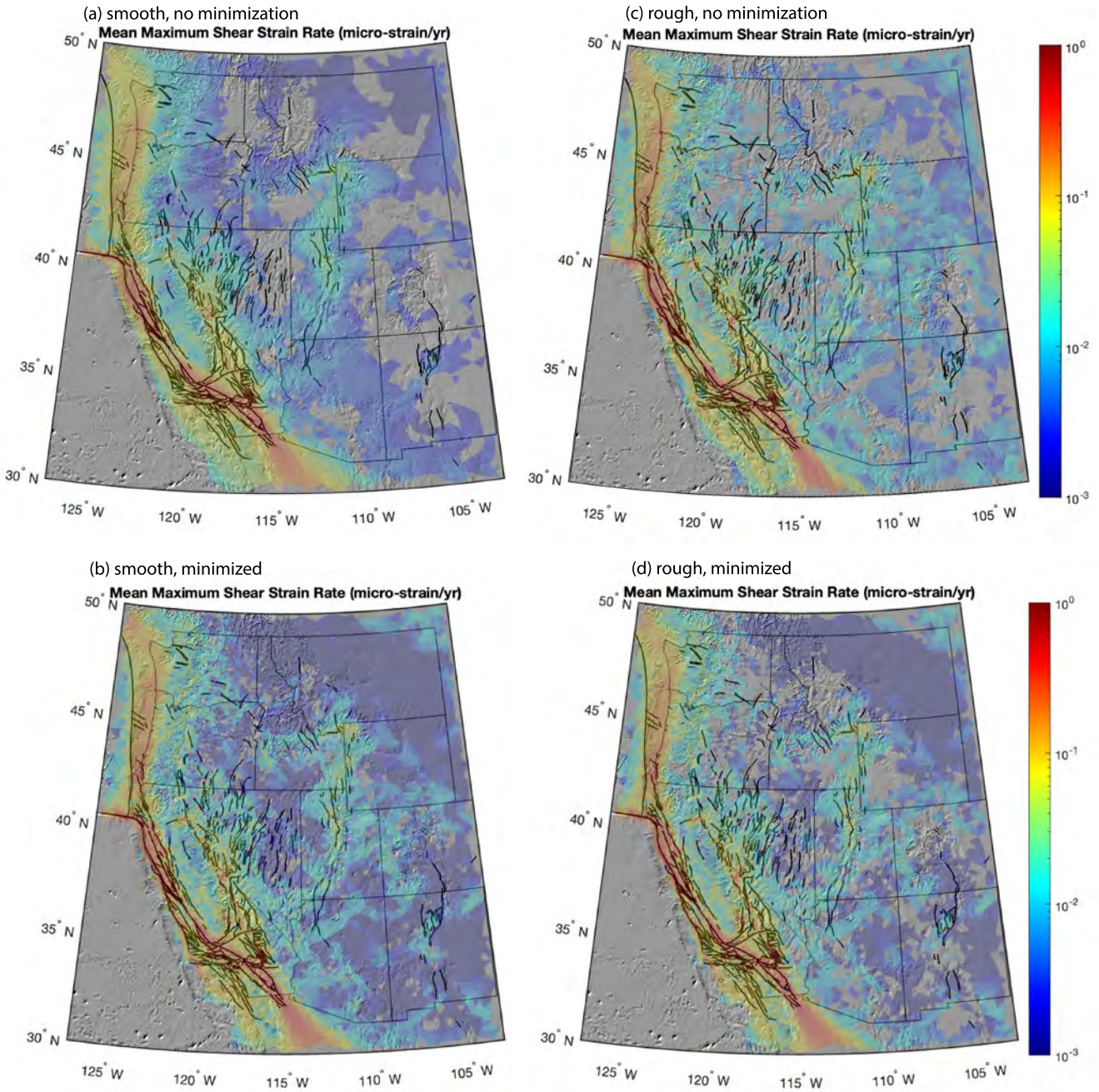

Figure 6. Mean maximum shear strain rate fields (mean of all realizations). Strain rate shown only for triangles in which at least one strain-rate tensor component is significantly different from zero at the 2 standard deviation level in panels (a, b) and the 1 standard deviation level in panels (c, d). (a) Maximum shear strain rate for smooth field without minimization. (b) same as panel (a) for smooth strain rate field with minimization. (c) same as panel (a) for rough strain rate field without minimization. (d) same as panel (a) for rough strain rate field with minimization.

only in cells in which at least one of the principal strain rates is significantly different from zero. Figure 9c shows the faulting style from the NSHM 2023 geologic deformation model. Here, faulting style is plotted as a modified rake angle, where the modified rake is the angle of inclination from the strike line, not differentiating sense (left or right) of lateral motion. At the broadest scale, the geologic and geodetic deformation styles are consistent and unsurprising. The Pacific Northwest and Western Transverse regions are dominated by geodetic reverse-faulting strain rate style, the major strike slip systems including the San Andreas, ECSZ, and Walker Lane show predominantly strike-slip style strain rate style, and normal-faulting style strain rate occurs in the CNSB and ISB.

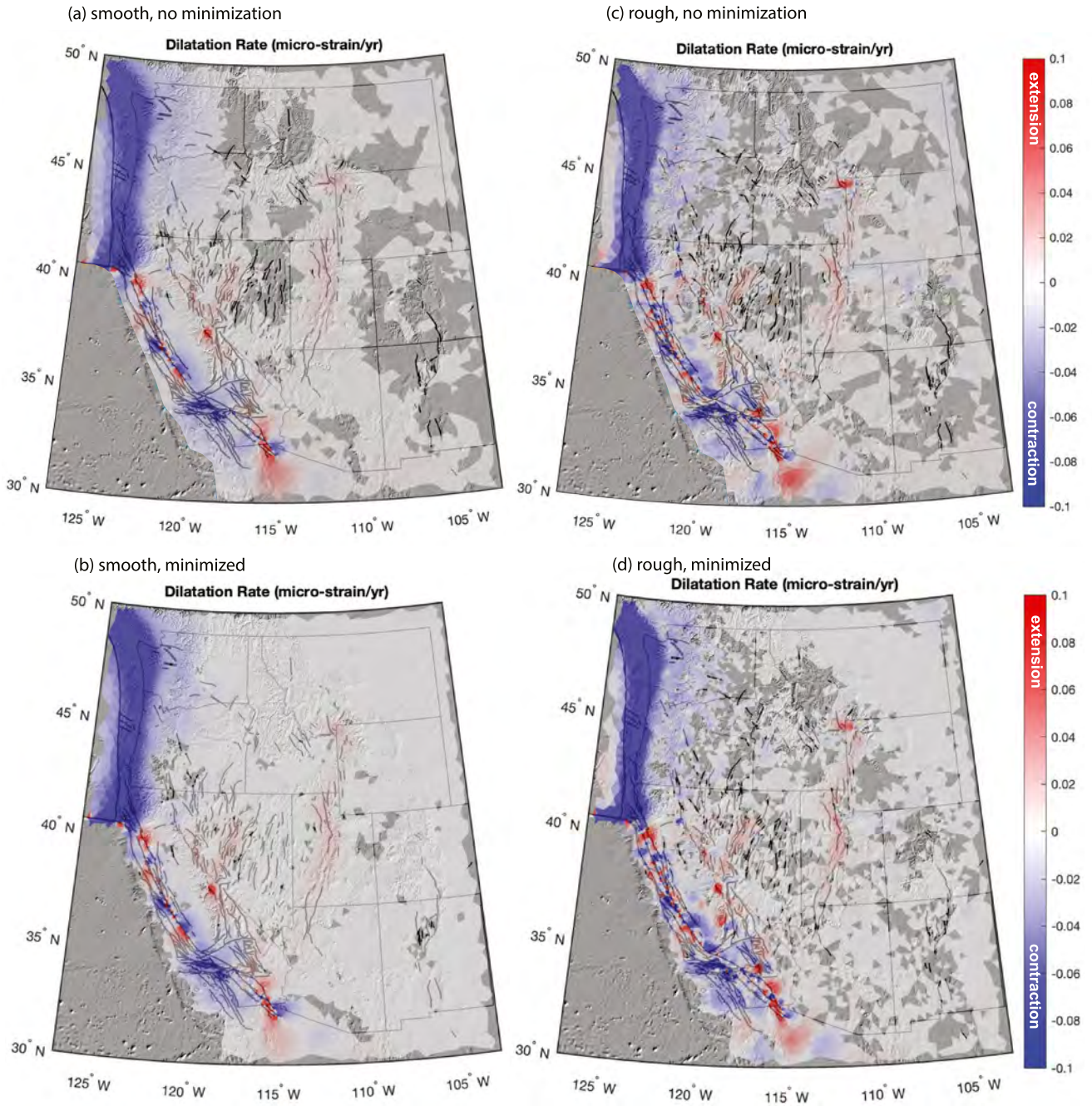

Figure 7. Dilatation rate fields (mean of all realizations). (a) Dilatation rate for smooth field without minimization. Dilatation rate shown only for triangles in which at least one strain-rate tensor component is significantly different from zero at the 2 standard deviation level in panels (a, b) and the 1 standard deviation level in panels (c, d). (b) same as panel (a) for smooth strain rate field with minimization. (c) same as panel (a) for rough strain rate field without minimization. (d) same as panel (a) for rough strain rate field with minimization.

However, within or surrounding these broad regions there are smaller pockets of strain rate style that are not consistent with the expected faulting style, for example, in eastern Nevada and surrounding the Rio Grande Rift. These deviations perhaps can be attributed to the transient elastic strain accumulation and release process in the crust, but this would require modeling to determine.

Profiles of mean maximum shear strain rates are shown in Figure 10. The profile locations are the same as velocity profiles in Figure 5. Strain rates from both of the smooth models are shown with red dots and circles and strain

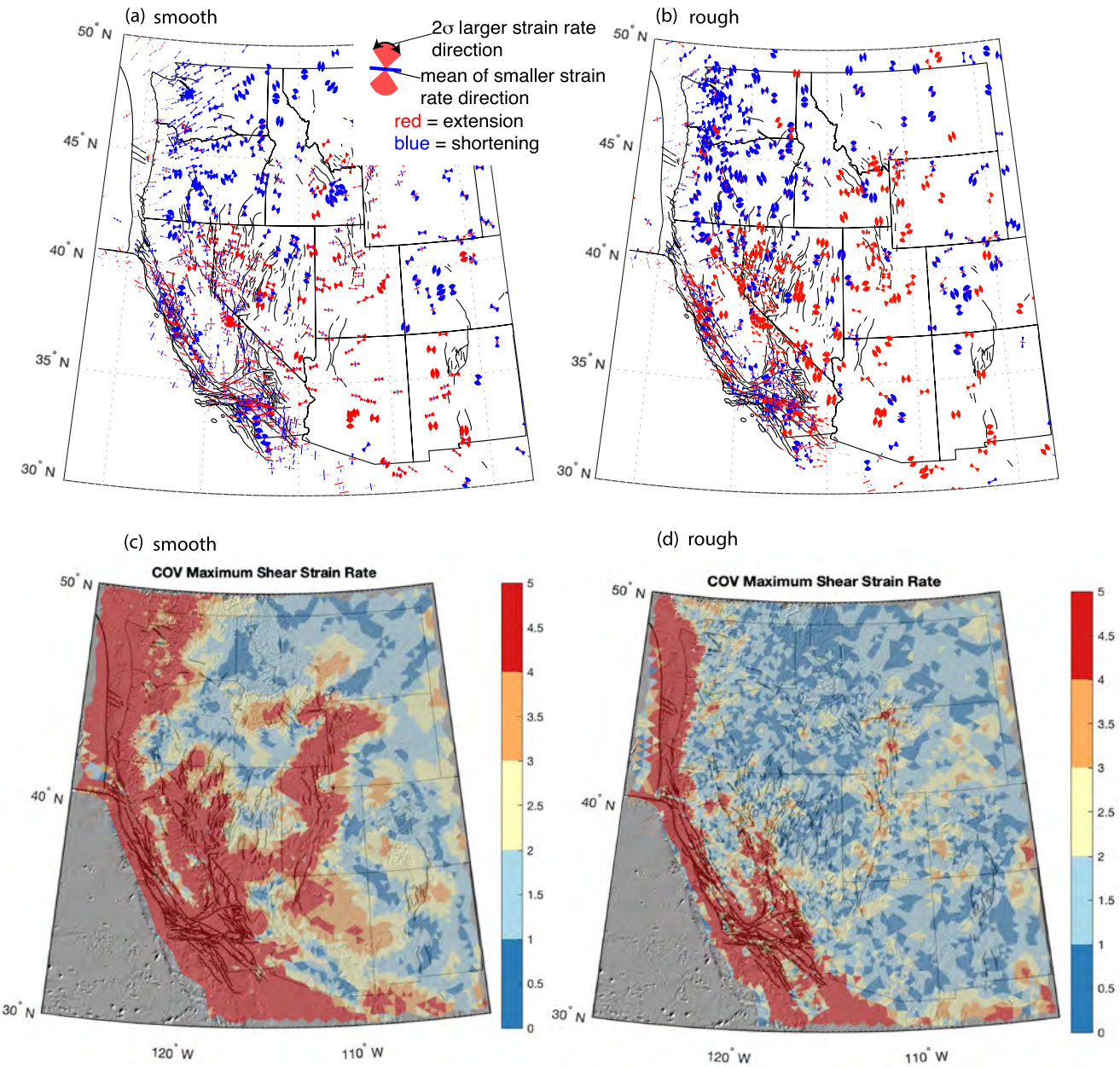

Figure 8. Uncertainties in strain rate field for both models without the minimization step. (a) Orientations of principal strain rate directions and uncertainties for smooth model. Wedges show 2-standard-deviation confidence intervals of the azimuth of the larger principal direction (absolute value) and the thin line shows the mean of the smaller strain rate orientation. (b) Orientations of principal strain rate directions and uncertainties for rough model. (c) Coefficient of variation (COV) of maximum shear strain rates (ratio of mean to standard deviation) for smooth model. (d) COV of maximum shear strain rates for rough model.

rates from both of the rough model are shown with black dots and circles. As expected, there is more spread along the profiles in the rough models. The magnitude of peak strain rates within deformation belts tend to be systematically lower in the smooth models, including the Wasatch front in profile 4, northern Walker Lane in profile 5, much of the Cascadia region in profile 6, and the Rio Grande Rift region in profile 7. These profiles illustrate the trade-offs introduced by regularization of the inversion of velocities for strain rate maps; the rougher maps, which fit the geodetic data largely within uncertainties (reduced chi-square values of 1–2) will likely produce spurious strain rates that may reflect noise or non-tectonic signals in the data, and the smoother models will tend to smooth through this noise and not fit the data as well at the expense of underestimating strain rates in highly deforming deformation belts. The minimized strain rate models display the expected feature of lower maximum

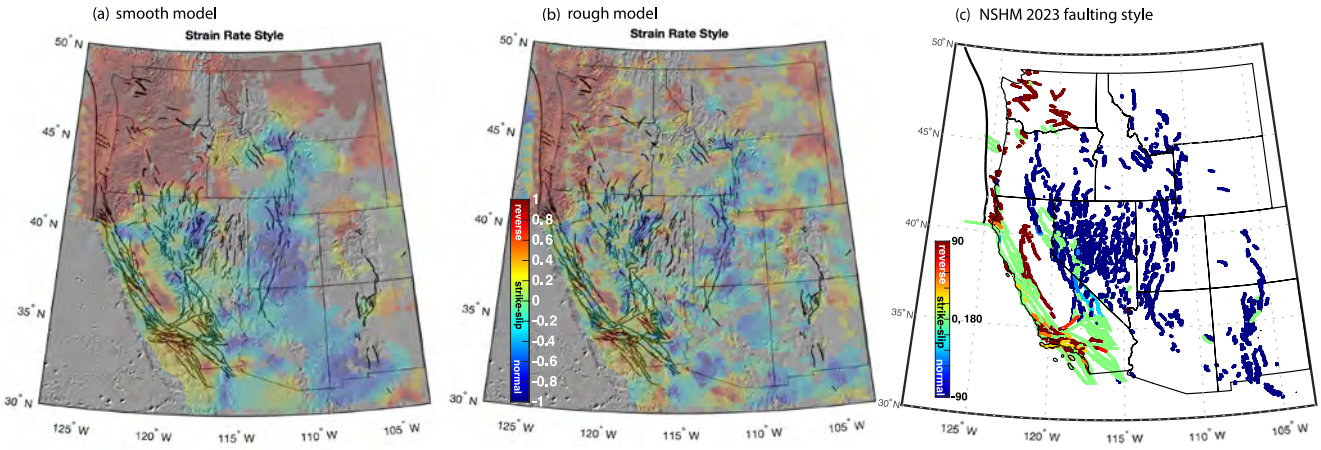

Figure 9. Comparison of geodetic strain rate style and geologic faulting style. (a) Strain rate style for smooth model without the minimization step. Style is defined as $(-\epsilon_1 - \epsilon_2)/(|\epsilon_1| + |\epsilon_2|)$. (b) same as panel (a) for rough model without the minimization step. (c). Faulting style from NSHM 2023 geologic model plotted as a modified rake angle that does not distinguish between sense of lateral slip, as explained in the text.

shear strain rates within many of the lower deforming rate regions. These low deforming rate regions show the widest spread in maximum shear rate indicating the epistemic uncertainty (model uncertainty introduced by regularization) is highest in these regions.

To further explore the epistemic uncertainty, Figure 11 shows the COV of mean velocity and mean maximum shear strain rate fields for the four models (smooth, rough, with and without minimization). Here, COV is simply defined as the ratio of the median value to the range. The top panels of Figure 11 show COV values in map view and the bottom panels show the COV as a function of the median value to illustrate the correlation of COV with magnitude of velocity and shear strain rate. I use a COV value of one as an arbitrary threshold above which I consider the value as having low epistemic uncertainty and below which the value has high epistemic uncertainty. Approximately 94% of the model domain area has velocity COV values above one, whereas about 59% of the model domain has maximum shear strain rate COV values above one. The scatter plots show that epistemic uncertainty in estimated strain rates is quite strongly correlated with the magnitude of strain rates. Maximum shear strain rates below about 10^{-2} micro-strain per year (10 nano-strain per year) are most uncertain with most COV values less than one.

There are two major general conclusions from this analysis: (a) Regularization (minimizing the magnitude of the body forces) introduces spatial smoothing that tends to lower peak strain rates in rapidly deforming belts, and (b) The epistemic uncertainty introduced by various regularization choices is quite large for maximum shear strain rates below about 10^{-2} micro-strain per year.

3.2.2. Regional Strain Rates

Figures 12–17 show zoomed-in results of the sub-regions of the western US defined in Figure 2a. The results in this section are from the rough inversion without the minimization step. In each of these figures, part (a) shows red (extension) or blue (shortening) wedges illustrating the 2-standard deviation range of the orientation of the larger of the two principal strain rate directions. Blue or red short line segments show the mean direction of the smaller principal direction. The line segments and wedges are scaled in size by the strain rate magnitude, as shown with the strain rate scale bar. Part (b) shows the strain rate style as in Figures 9a and 9b. Part (c) compares the azimuths of maximum horizontal shortening rate and maximum horizontal stress. The red/blue uncertainty wedges are unscaled versions of the wedges in part (a) and the short black line segments show maximum horizontal stress taken from the World Stress Map (Heidbach et al., 2016) as well as Levandowski et al. (2018). Spatially-smoothed azimuths (30-km-radius moving circular median) of maximum shortening rate and maximum horizontal stress are also compared in part (c).

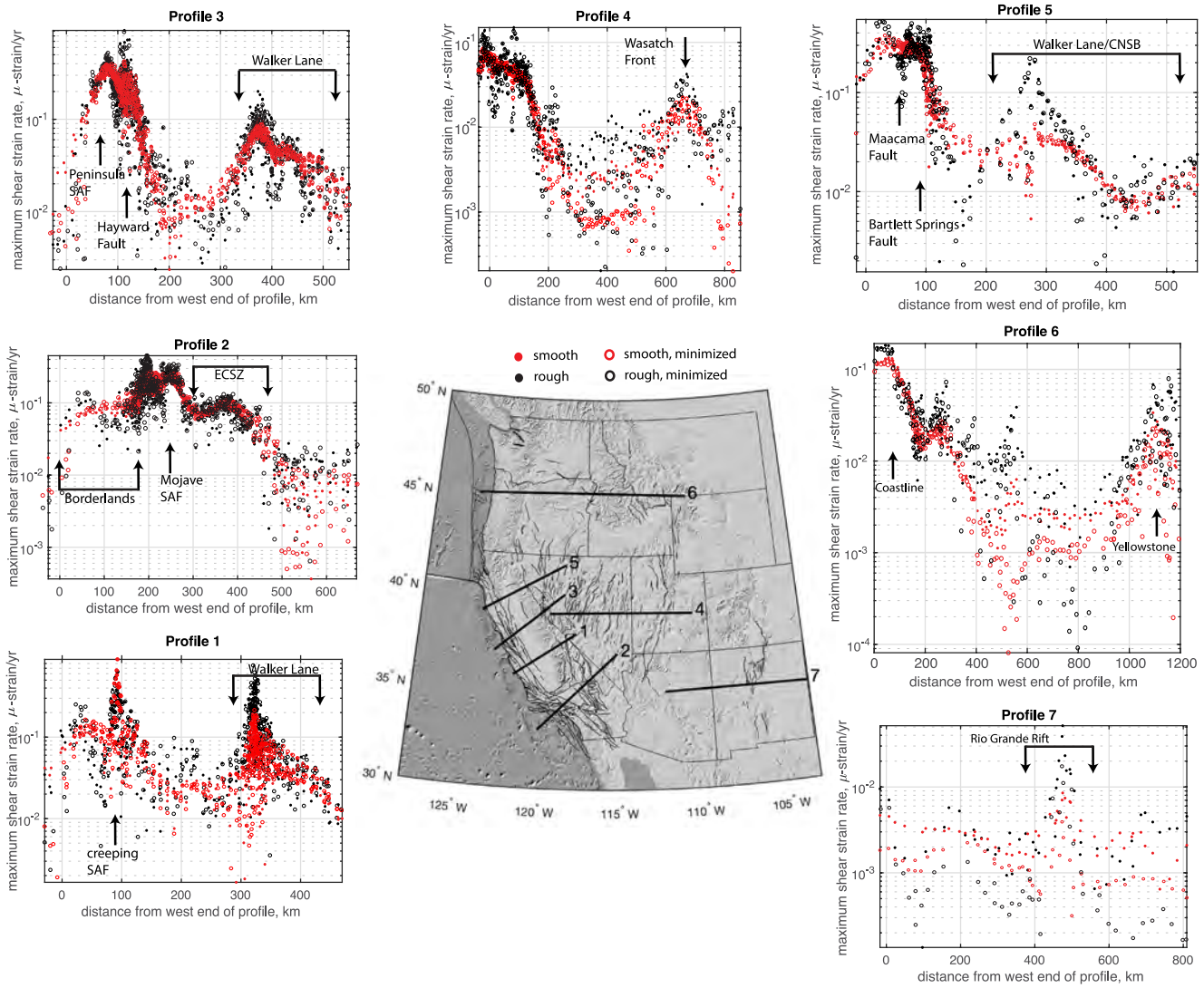

Figure 10. Profiles of mean maximum shear strain rates for all four inversions (both smooth and rough models, with and without minimization). Profile locations are same as in Figure 5. Red dots and circles show smooth strain rate models and black dots and circles shown rough models. Locations of major fault zones are indicated.

3.2.2.1. Pacific Northwest

Unsurprisingly, the strain rate field in the Pacific Northwest (Figure 12a) is dominated by strain associated with interseismic locking on the Cascadia subduction interface with approximately E-W oriented maximum horizontal shortening rates. The strain rate style is largely consistent with reverse faulting. The horizontal maximum shortening rates throughout the Pacific Northwest are nearly perpendicular to the N-S oriented maximum horizontal stress orientations (Figure 12c).

Based on the magnitude and orientation of the maximum horizontal shortening rate, I have constructed the dashed line in Figures 12a–12c to show the interpreted eastward extent of strain rates associated with interseismic coupling on the subduction interface. This coupling strain extends as far as 500 km inland from the trench.

3.2.2.2. Northern San Andreas System

Figure 13 compares stress and strain rate orientations for northern California. At the southern end of the map (south of the San Francisco Bay area), the strain rates are largely localized across the SAF and Calaveras Fault. The strain belt broadens out to the north where it is spread across the sub-parallel San Andreas, Maacama, and Bartlett Springs strike-slip faults. The strain rate style parameter largely hovers near zero, indicating strike-slip

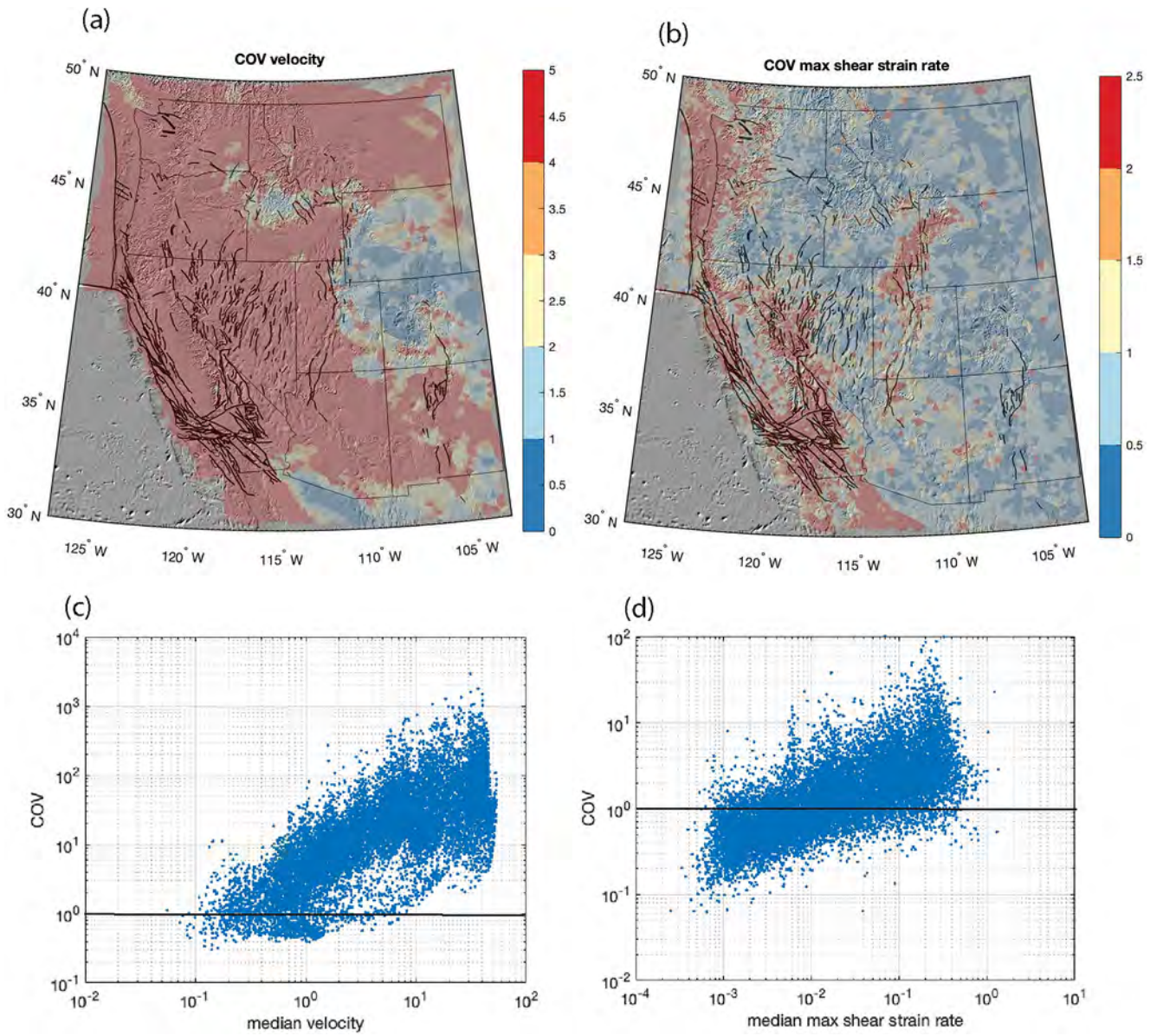

Figure 11. (a) Coefficient of variation (COV) of velocity and maximum shear strain rate. (a) COV of velocity models. COV is the median divided by the range of the four mean fields (smooth, rough, smooth and minimized, rough and minimized). (b) same as panel (a) for maximum shear strain rate. (c) COV of velocity at all model nodes as a function of the median value. (d) COV of maximum shear strain rate at all model nodes as a function of the median value.

style strain rate across the major faults. Small pockets of normal and reverse style strain rate may be associated with along-strike gradients in near-surface fault creep, which is abundant in this region. Reverse style strain rates east of the Concord-Green Valley fault system is consistent with reverse slip on faults bounding the west side of the central valley (Figure 9c).

There is a small, but systematic difference in orientation of the maximum horizontal shortening strain rate and maximum horizontal stress. Along the major strike-slip faults (named faults in Figure 13b), the maximum shortening rates are systematically rotated about 10–15° to the north relative the maximum horizontal stress directions.

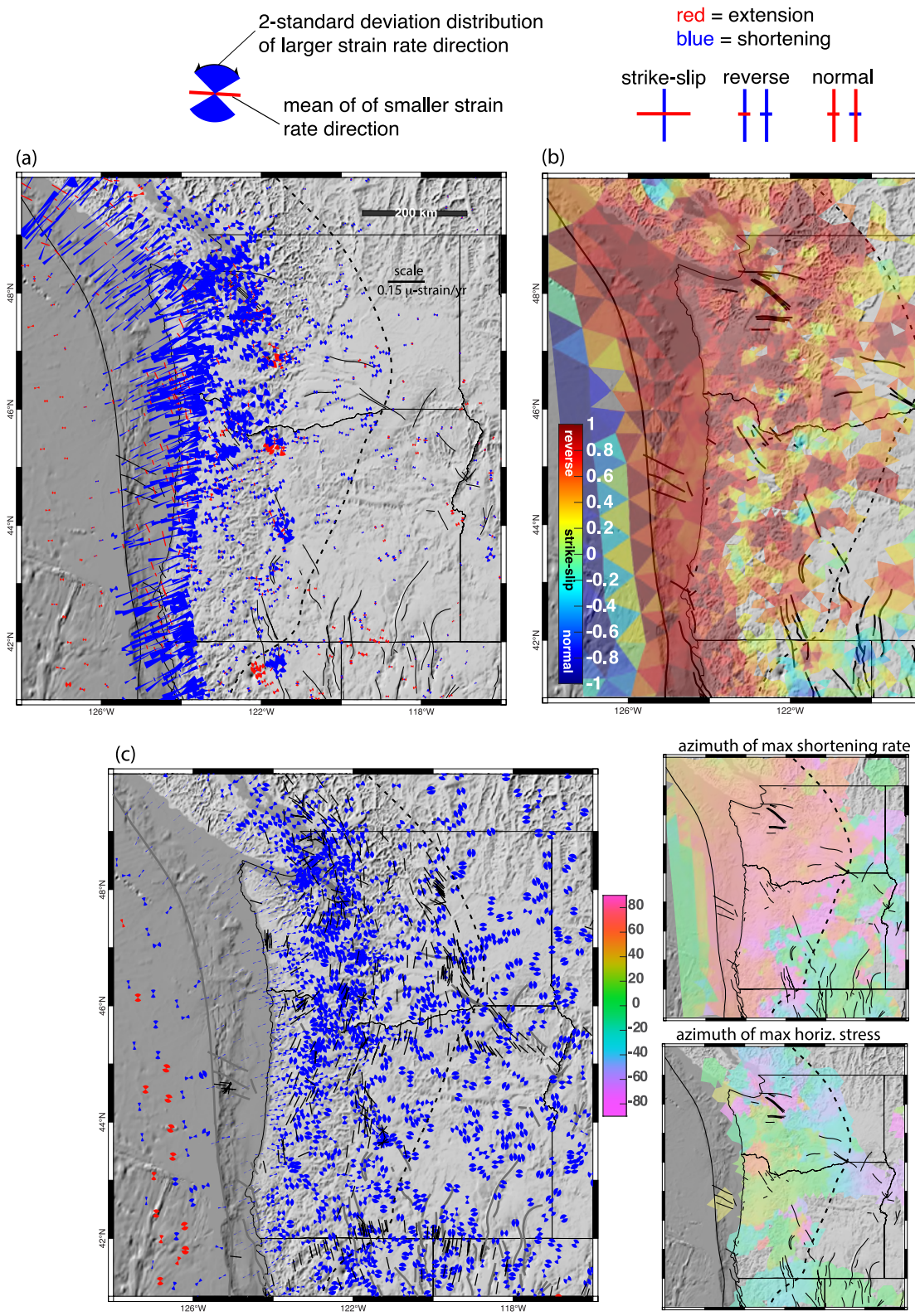

Figure 12.

3.2.2.3. Central San Andreas System

Figure 14 compares stress and strain rate orientations in central California. Strain rates are relatively high along the Carrizo section of the SAF but low along the creeping central section. Along the Carrizo section the strain rate style is largely strike-slip but alternating quadrants of reverse and normal style strain rates (designated with white dashed circles in Figure 14b) occur at the northern and southern ends of the central creeping section of the SAF, likely due to the termination of surface fault creep. Reverse-style strain rates NE of the SAF are consistent with reverse-slip faulting on San Jaoquin valley bounding faults (see Figure 9c).

Like in northern California (Figure 13), there is a systematic difference in orientation of the maximum horizontal shortening strain rate and maximum horizontal stress. Along the SAF, the maximum shortening rates are systematically rotated about 20–30° to the north relative the maximum horizontal stress directions.

3.2.2.4. Southern California

Figure 15 compares stress and strain rate orientations in southern California. The highest strain rates are along the SAF system, the strike-slip San Jacinto fault and within the fold-thrust belt of the Western Transverse Ranges (WTR). Lower, but significant strain rates occur across the ECSZ. Strain rate style along the SAF hovers around zero, consistent with strike-slip faulting. Reverse-faulting style strain rate occurs in the Western Transverse Range, consistent with slip on reverse faults in the fold-thrust belt. Alternating quadrants of reverse and normal strain rate style in the ECSZ (designated with white dashed circles in Figure 15b) is consistent with postseismic relaxation following the 1992 Landers and 1999 Hector Mine earthquakes (e.g., Liu et al., 2020; Pollitz et al., 2001; Pollitz, 2015).

There are differences in azimuth of maximum horizontal shortening rate and maximum horizontal stress along the SAF (Figure 15c). The maximum horizontal shortening direction is rotated systematically 10–30∘counter-clockwise from the trend of maximum horizontal stress. This result is generally consistent with the findings of Yang et al. (2013).

3.2.2.5. Northern Basin and Range

Figure 16 compares stress and strain rate orientations in the northern Basin and Range region. Here, the highest strain rates occur within the CNSB and WLB. The normal faulting strain rate style and extension direction in the CNSB is consistent with faulting style in that region (Figure 9c). Mixed strike-slip and normal style strain rate in the WLB is consistent with the observed transtensional faulting.

The maximum horizontal strain rate and stress are well-aligned in these regions. The strain rates are lower east of the CNSB and largely not significantly different from zero.

3.2.2.6. Intermountain Seismic Belt

Figure 17 compares stress and strain rate orientations along the eastern edge of the northern Basin and Range region. The strain rates are highest within the Intermountain Seismic Belt (ISB; see Figure 1). Extension rates are generally oriented perpendicular to the arcuate trend of the IWSB and the normal faulting strain rate style is consistent with the fault slip style.

Across the Wasatch Fault Zone in northern Utah and at the southwestern end of the IWSB, the orientation of maximum horizontal shortening rates are consistent with maximum horizontal stress orientations. Strain rates are low and noisy across the Hurricane and Toroweap faults.

Figure 12. Strain rates and maximum horizontal stress orientations in Cascadia region (rough inversion). Dashed black curve shows approximate eastward extent of strain rate associated with subduction zone coupling. (a) Principal strain rate directions showing 2 standard deviation uncertainty wedges on the larger magnitude strain direction. Short red or blue line segments show mean orientation of smaller principal strain rate direction. Length of line segments and radius of wedges proportional to strain rate magnitude. Red indicates extension and blue indicates shortening. (b) Strain rate style as in Figure 9. (c) Maximum horizontal stress orientation shown with black line segments. Red or blue uncertainty wedges same as in panel (a), but not scaled in size to magnitude. Color maps to the right show orientation of maximum horizontal strain rates and principal stresses. Strain rate and stress orientations are smoothed with a moving 30-km-radius circular median window.

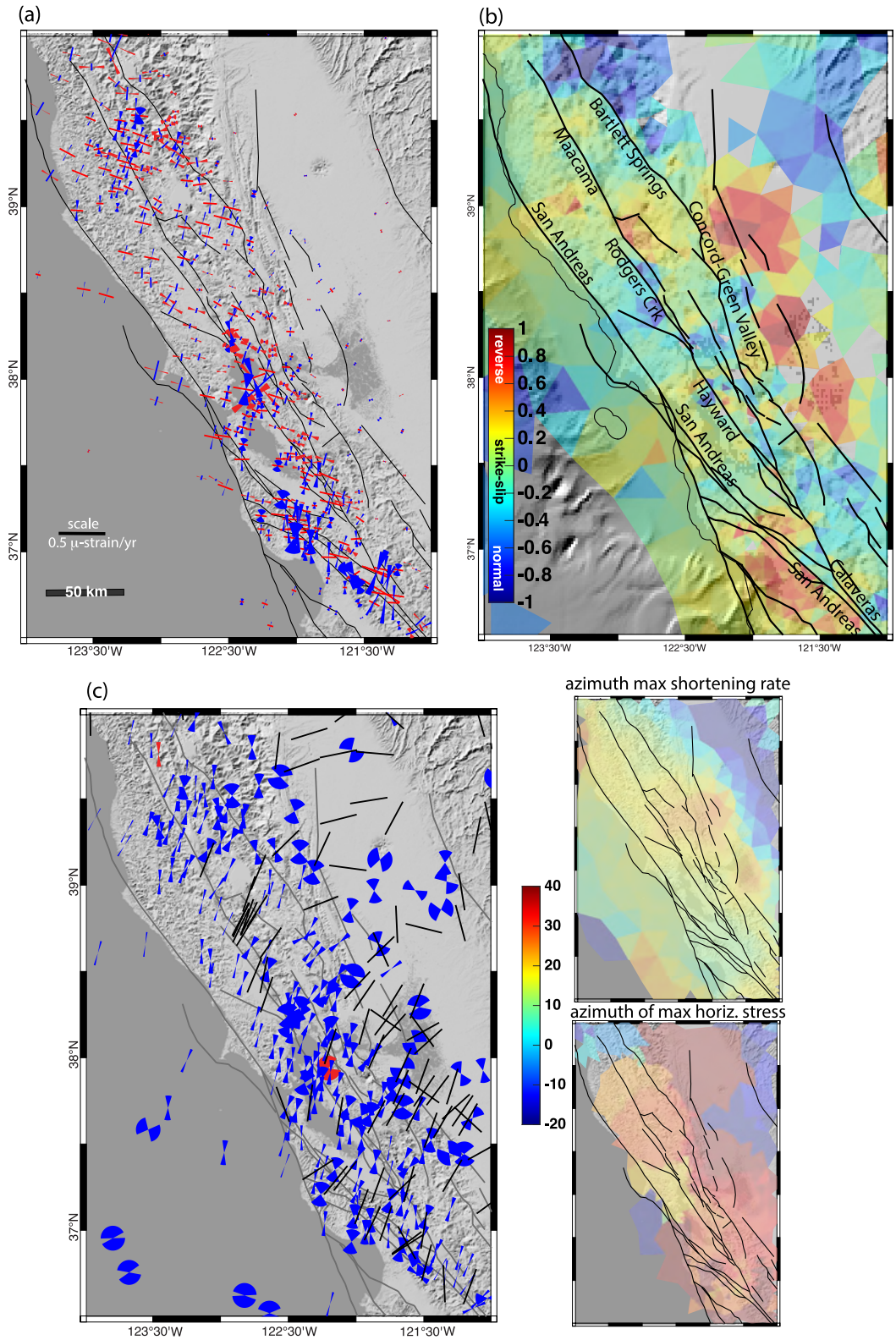

Figure 13. Same as Figure 12 for northern California region.

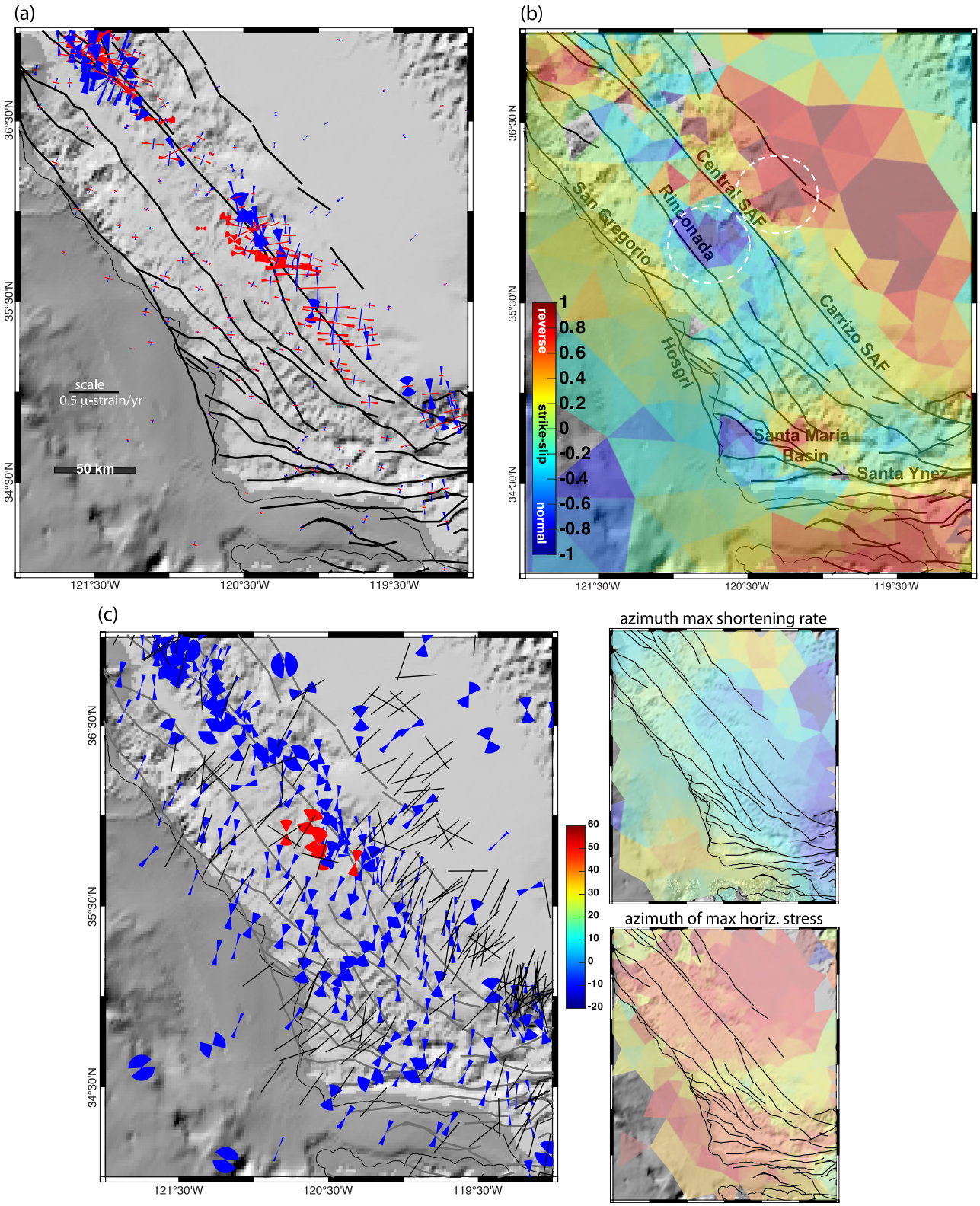

Figure 14. Same as Figure 12 for central California region.

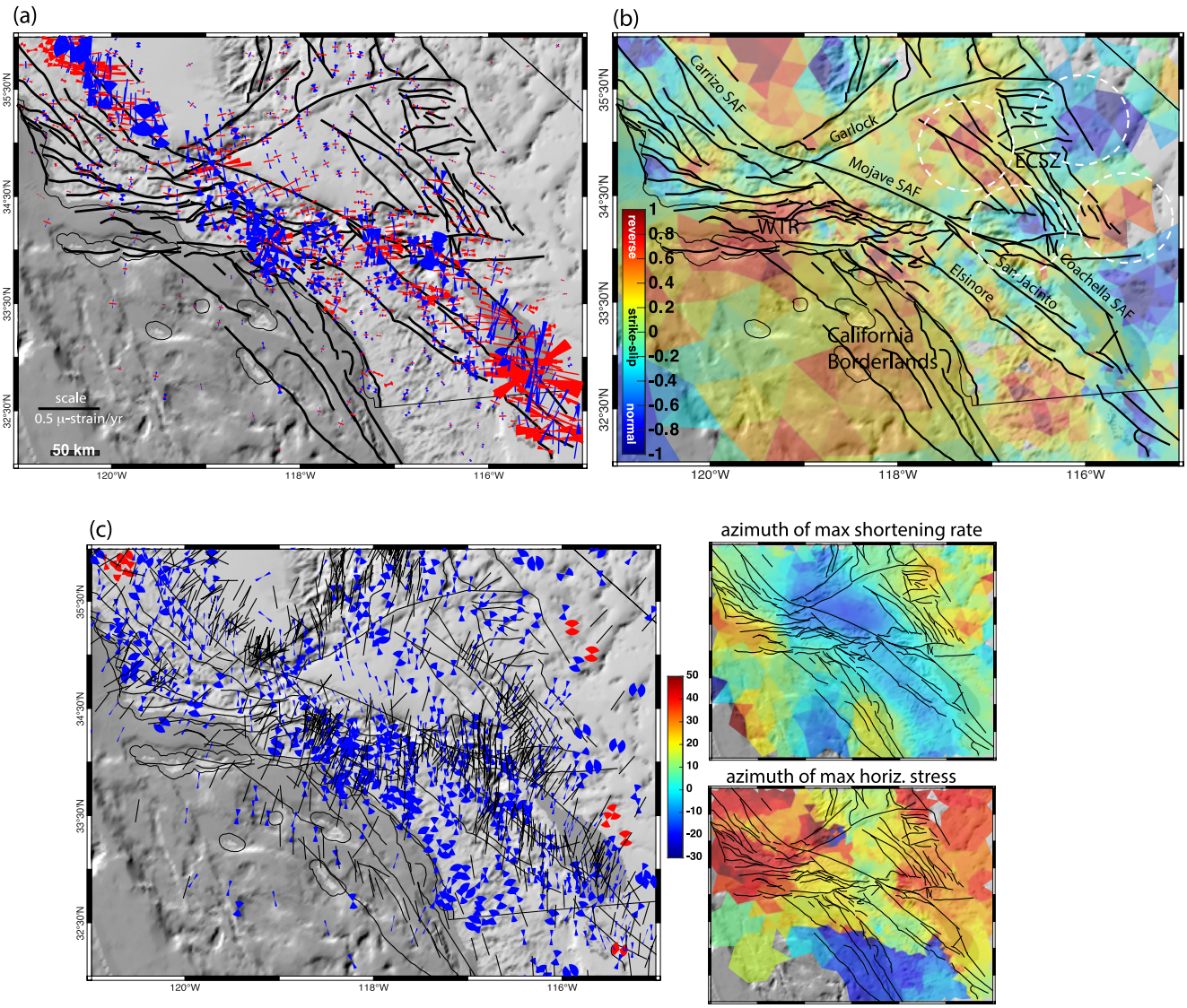

Figure 15. Same as Figure 12 for southern California region.

3.3. Comparison of Strain Rate and Stress Orientations

Figures 18a and 18b summarizes the principal strain rate and stress orientations discussed in the previous section. Differences between stress and strain rate directions are shown in Figure 18c. Systematic differences in orientations of maximum horizontal shortening rate and stress occur in the Cascadia subduction zone region and along the entire SAF system. The principal shortening rate directions deviate by more than 40° and up to 90° from maximum horizontal stress directions in the Pacific Northwest (Figure 18d). Along the SAF system and the southern half of the ISB, the geodetically derived maximum shortening rate directions are systematically rotated 25–40° counterclockwise from the maximum horizontal stress orientations.

Principal strain rate and stress orientations need not be the same. Stress orientations are computed from borehole breakouts and slip on faults which respond to the total stress in the crust and are best associated with strain release processes. Conversely, strain rates are instantaneous measures of the change in strain accumulation in the crust with time. However, some studies have used maximum horizontal compressive stress orientations as a proxy for maximum shortening rate directions (e.g., Bird, 2009; Flesch et al., 2005; Shen & Bird, 2022).

The strain accumulation process in the Pacific Northwest/Cascadia is dominated by coupling on the subduction interface and is clearly different from the stress release process on crustal faults in the region. This stress-strain

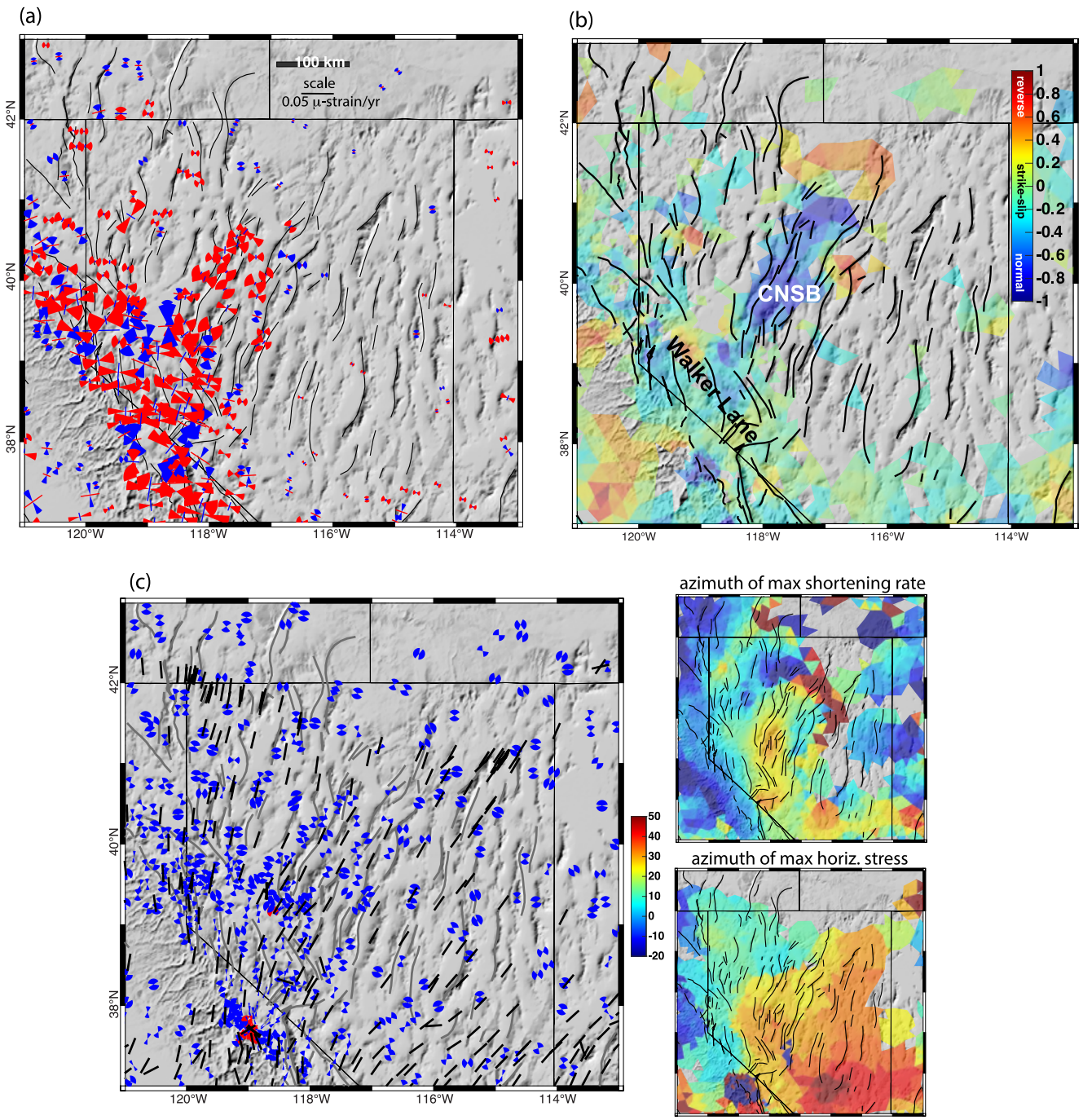

Figure 16. Same as Figure 12 for northern Basin and Range region.

rate relationship has been noted previously in Cascadia as well as at the Nankai subduction zone in southwest Japan (Townend & Zoback, 2006; Wang, 2000). Along the SAF system, the principal strain rates are oriented approximately 45° to the fault trace normals whereas the maximum horizontal stresses are oriented closer to perpendicular to the fault traces (approximately 0–30° from the normal). Much has been made of this high orientation of maximum horizontal stress to the SAF (e.g., Hardebeck & Hauksson, 2001; Townend & Zoback, 2001, 2004). The orientation of maximum horizontal strain rate is consistent with interseismic strain rate accumulation on vertical strike-slip faults (under simple shear parallel to faults the maximum horizontal shortening rate is rotated 45° from the fault).

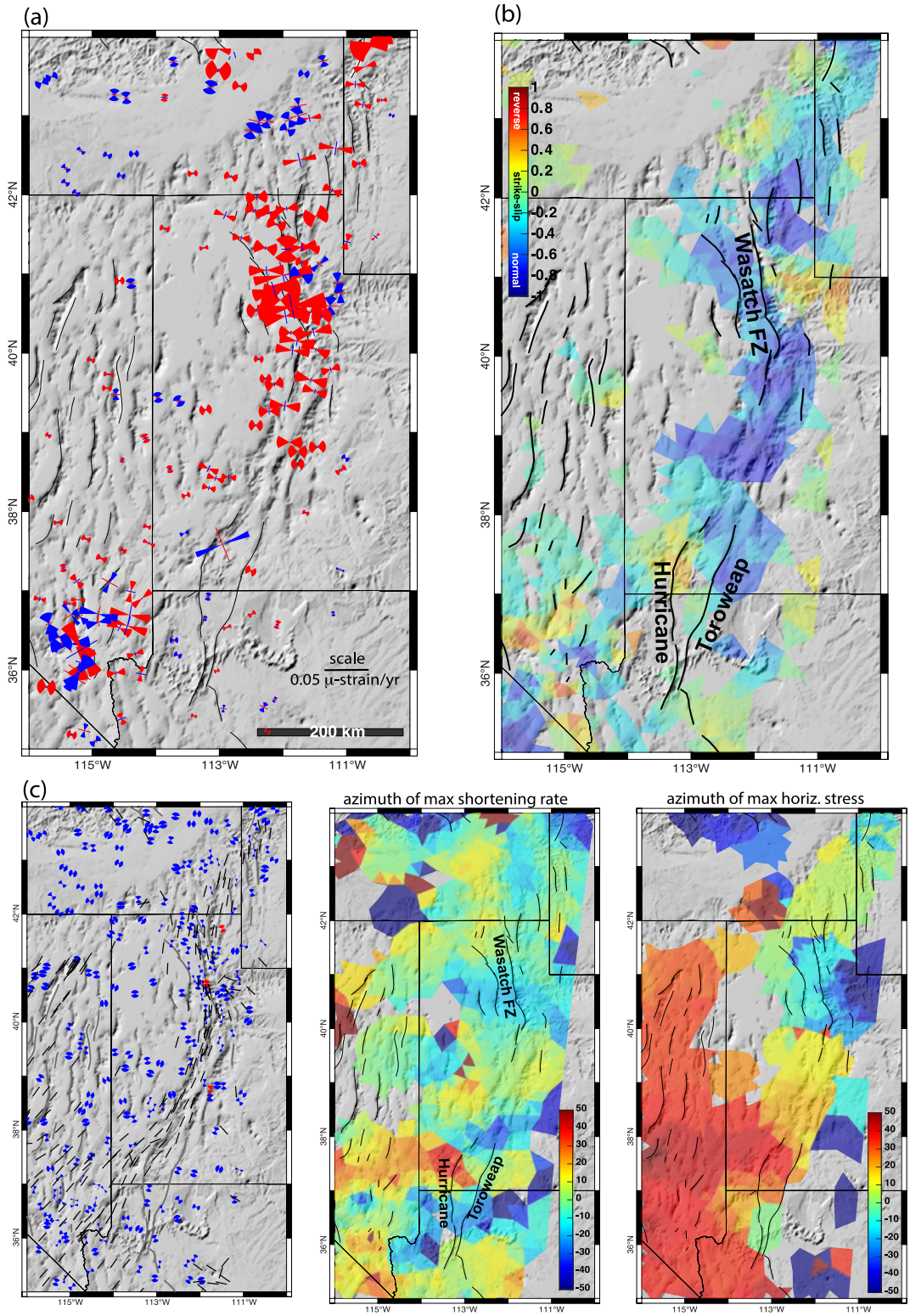

Figure 17. Same as Figure 12 for Intermountain Seismic Belt region.

The simplest explanation for the systematic differences in stress and strain rate orientations is that the contribution to the total crustal stress due to interseismic coupling along faults and the Cascadia subduction interface is small compared to other tectonic loads. For example, Humphreys and Coblentz (2007) showed that principal stress

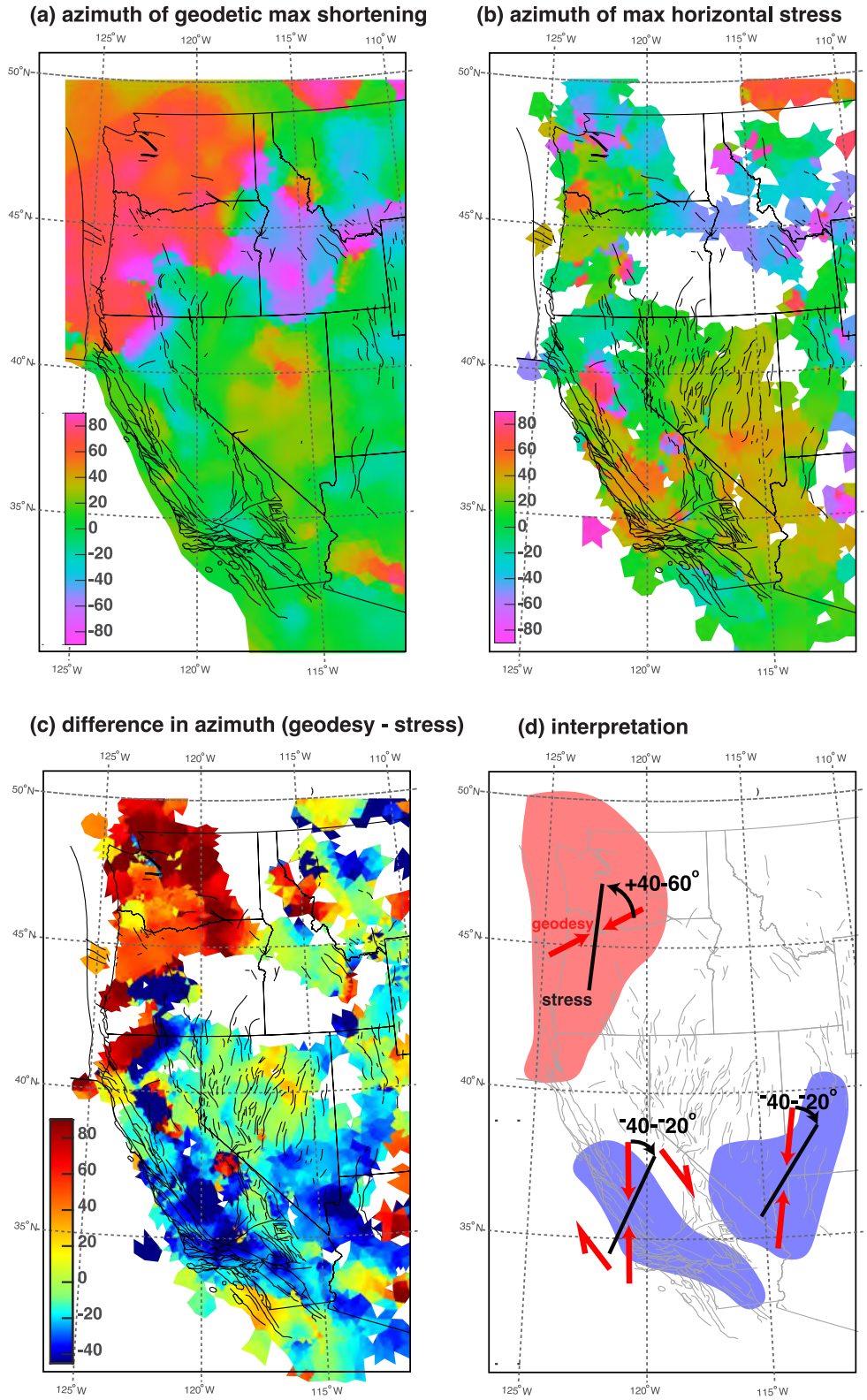

Figure 18.

orientations in North America can be explained well with plate boundary loads and gravitational potential loads. Humphreys and Coblentz (2007) and global dynamic models of Ghosh et al. (2013) and Ghosh and Holt (2012) predict roughly N-S oriented maximum horizontal stresses in the Pacific Northwest. Humphreys and Coblentz (2007) computed depth-averaged crustal shear stresses of about 40 MPa along the San Andreas margin. However, a number of studies of apparent coseismic rotations in stress orientation suggest low crustal stress levels of similar magnitude to coseismic stress drops (Hardebeck & Okada, 2018). Further study of the systematic rotation of the maximum shortening rate relative to the stress directions might provide additional constraints on the total stress in the crust.

3.4. Comparison of Geologic and Geodetic Moment Rates

In this section I return to the moment rate calculations computed geodetically and from geologic slip rates as illustrated in Figure 2. Savage and Simpson (1997) proposed that the minimum scalar moment rate can be related to surface principal strain rates, ϵ_1 and ϵ_2, through

$$M_0 = 2\mu HA \times \max(|\epsilon_1|, |\epsilon_2|, |\epsilon_1 + \epsilon_2|) \tag{16}$$

where μ is the elastic shear modulus, H is the assumed seismogenic thickness of the crust, and A is the surface area over which the strain rates can be reasonably assumed to be uniform. For this analysis, I assume $H = 15$ km and $\mu = 30$ GPa.

Figures 19a–19c compares geodetic moment rates computed from strain rates with moment rates derived from the geologic deformation model. For the sake of visual comparison, the geodetically derived moment rates are computed by taking a 30-km radius moving circular window mean of the moment rates in each triangle of the mesh and the geologic moment rates are similarly computed by taking a 30-km radius moving circular window mean of the moment rates computed at the center of all fault sections in the 2023 NSHM geologic deformation model. The source area for the geologic moments are computed using the NSHM 2023 fault model dip and assuming a seismogenic depth of 15 km. It is evident from examination of Figures 19a–19c that the geologic moment rates are systematically lower than the geodetic moment rates over large areas of the western US, especially outside of California. It is important to note that the geologic moment rate calculation does not include moment associated with the Cascadia subduction zone.

To more closely examine the comparison of geologic and minimum geodetic moment rates, I plot summed moment rates for the four models by region in Figure 19d using the tectonic regions defined in Figure 2a. Because moment is a non-negative quantity (absolute value in Equation 16), noisy, near-zero principal strain rates with distributions that include positive and negative values tend to amplify the total moment over a region rather than cancel out. Thus, I compute a conservative regional moment rate by setting to zero any strain rate components where the mean of the distribution does not exceed zero by more than one standard deviation. We see a similar relationship between geologic and geodetic moment rates that was identified in Figure 2. The geodetic moment rates are higher than the geologic model moment rates for all regions except the three highest moment rate regions (WTR, Southern SAF, Northern SAF). The minimized strain rate models are comparable to the geologic moment rate in the Rio Grande region. Figure 19e summarizes all moment rate calculations discussed in this paper. The geodetically derived moment rates from this study encompass the Kreemer and Young (2022) rates nearly completely and are above the range of NSHM 2023 on-fault moment rates in all of the lower deforming regions except the Rio Grande region where the geodetically derived moment rates are highly uncertain. The geodetically derived moment rates are also tend to the high end or higher than the range of total NSHM 2023 deformation model rates, accept again for the Rio Grande Region.

It is not immediately evident from this study why this systematic pattern of high geodetically derived moment rates emerges for the low strain rate regions. One possible explanation is that the geodetic moment rates are

Figure 18. Comparison of maximum horizontal strain rate (a) and stress directions (b). (c) Plot of difference in azimuths. Systematic differences are evident including clockwise rotation of maximum horizontal stress in Cascadia relative to maximum horizontal strain rate directions and counterclockwise rotation along much of the San Andreas Fault system. (d) Red arrow pairs represent maximum shortening rate direction and heavy black line represents maximum horizontal stress direction. Sense and degree of systematic rotations are indicated.

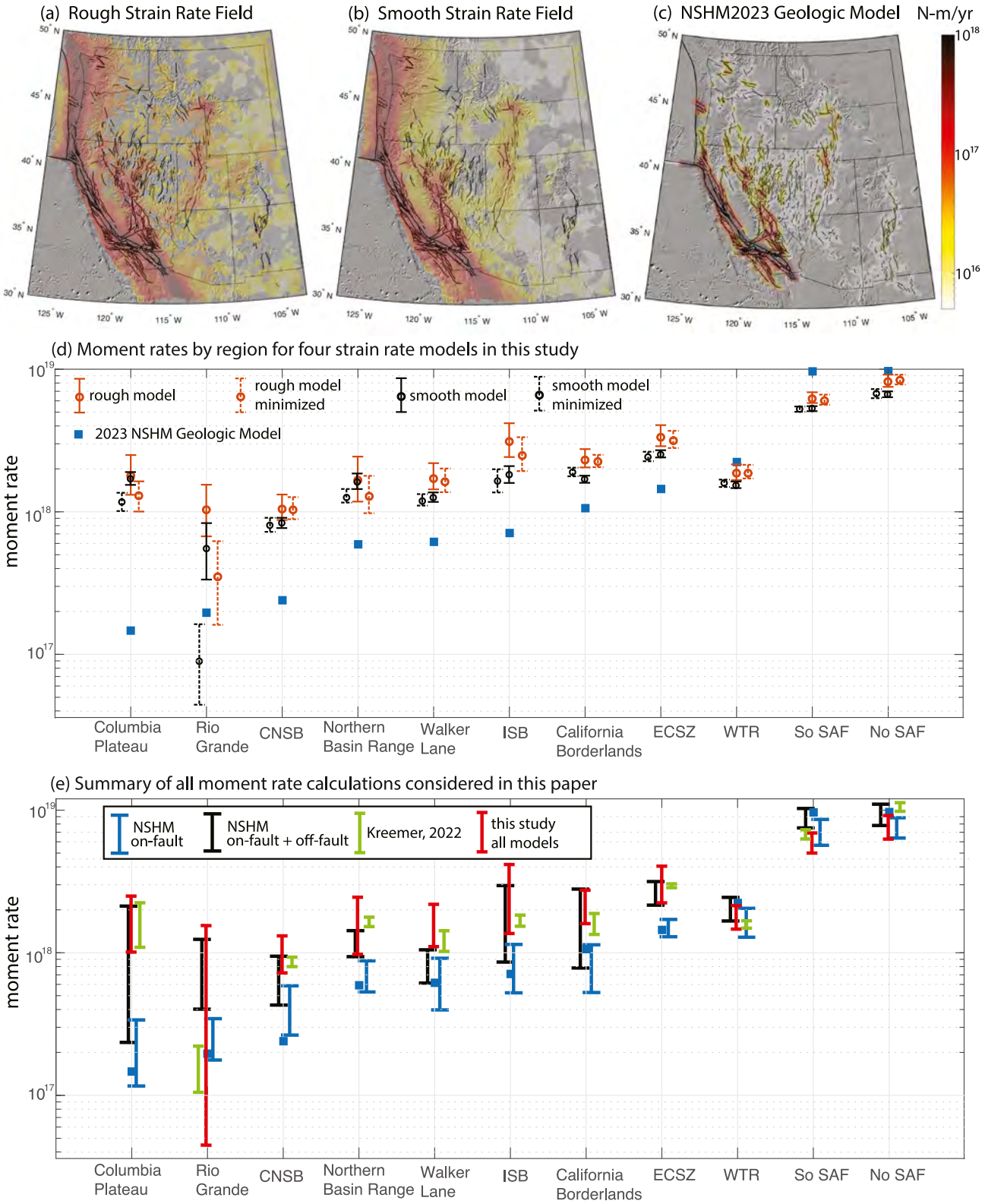

Figure 19.

systemically over-estimated within the lower deformation rate regions because moment is a non-negative quantity and noise/errors in the estimated strain rate field all sum to a positive value, although I have accounted for this to some extent by computing a conservative moment rate as described above. Another possible explanation is that the geodetic data record strain rate due to faults that are not in the NSHM 2023 geologic deformation model, or the NSHM model systematically under-assigned slip rates to faults in the low deformation regions. It is also possible that a portion of the geodetic moment rate is not released by slip on faults and instead manifests as distributed inelastic deformation through the crust (e.g., Bird, 2009; Herbert et al., 2014). It is possible that the systematically lower geodetic moment rates in the three highest moment rate regions can be attributed to the algorithm as Savage and Simpson (1997) note that their method (Equation 16) provides a minimum estimate of moment rate. It is also possible that the 2023 NSHM geologic deformation model systemically over estimates slip rates in these higher deformation regions. The explanation of systematic differences in geologic and geodetic moment rates is beyond the scope of this paper but deserves further exploration in the future.

4. Conclusions

I have developed an elasticity-based method for estimating velocity and strain rate fields and uncertainties that builds on the methods of Haines et al. (2015) and the gpsgridder method (implemented in GMT) by Sandwell and Wessel (2016). As in these previously published methods, I compute a continuous deformation field by solving for a distribution of body forces in a thin elastic plate. I also allow for discontinuities across creeping faults using the solution for dislocations in a thin elastic plate. I compute uncertainties in strain rate field propagated through from both formal uncertainties in the GNSS derived velocity field and uncertainty in spatial smoothing of the body forces. To further explore epistemic uncertainties introduced by regularization choices, I computed four different strain rate maps with varying levels of damping as well as strain rate minimization in low-deforming regions. I find that the epistemic uncertainty is generally higher than the uncertainty of any single strain rate model, especially in regions with maximum shear strain rates less than 10^{-2} micro-strain per year.

I compare principal strain rate directions with directions of maximum horizontal stress and find systematic differences in orientations in the Pacific Northwest region that is influenced by Cascadia subduction and along much of the SAF system. In the Pacific Northwest, the maximum shortening rate directions are consistent with strain rates expected due coupling on the Cascadia subduction interface whereas the maximum horizontal stress orientations are rotated counterclockwise 40–90° relative to the strain rates and generally consistent with north-south shortening in the Yakima Fold and Thrust Belt. Along the SAF system the maximum horizontal shortening rates are oriented roughly 45° from the strike of major strike-slip faults, consistent with simple shear due to interseismic coupling on faults. The maximum horizontal stresses are rotated systematically 25–40° clockwise (closer to fault normal) relative to the strain rates.

I also compare the total geodetic moment calculated over tectonic regions with the moment rates in the NSHM 2023 deformation models. The geodetic rates are higher than the on-fault moment rates for all regions except the three highest moment rate regions (WTR, Southern SAF System, Northern SAF System). The geodetic moment rates are lower than the on-fault moment rates for the three highest moment rate regions. The total geodetic moment rates are comparable to the total (on-fault + off-fault) moment rates in the geodetically-based NSHM deformation models. This suggests that either the moment-rates on faults are underestimated in the NSHM, perhaps because the model is missing faults, or that a sizable (∼30%) portion of the total moment release in the western US occurs as distributed deformation in the areas of the crust between faults.

Figure 19. Geodetic and geologic moment rates (N-m/yr). (a–b) Spatially averaged (30-km radius moving circular mean window) geodetic moment rates computed as described in the text. Only moment rates with mean exceeding zero by two standard deviations are shown. (c) Spatially averaged (30-km radius moving circular mean window) geologic moment rates computed from the NSHM 2023 geologic deformation model as described in more detail in the text. Note that the geologic model does not include slip on the Casadia subduction zone interface while the geodetic moment rates include strain due to this process. (d) Comparison of geodetic and geologic model moment rates by regions defined in Figure 2a. Both geodetic and geologic moment rates assume a 15-km depth seismogenic zone. Geodetic moment rates are computed using Equation 16 and geologic rates are computed using the preferred slip rates and fault geometry from the NSHM 2023 geologic deformation model (Hatem et al., 2022). (e) Summary of all moment rates by region presented in this paper.

Data Availability Statement

The GNSS derived velocity field used in this study is available in Zeng (2022). Stress orientation data used in this study are available from the World Stress Map (Heidbach et al., 2016) as well as Levandowski et al. (2018). The computer code, BforStrain, is available in (Johnson, 2023b). The strain rate and velocity field realizations for the four inversions in this study are available in (Johnson, 2023a).

Acknowledgments
The author thanks Jeremy Maurer at Missouri University S&T for discussions about computing strain rate from geodetic data. This research was supported by the Southern California Earthquake Center (Contribution No. 11842) and USGS NEHRP Grant award G22AP00263. SCEC is funded by NSF Cooperative Agreement EAR-1600087 and USGS Cooperative Agreement G17AC00047.

References

Beavan, J., & Haines, J. (2001). Contemporary horizontal velocity and strain rate fields of the Pacific-Australian plate boundary zone through New Zealand. *Journal of Geophysical Research: Solid Earth*, *106*(B1), 741–770. https://doi.org/10.1029/2000JB900302

Bird, P. (2009). Long-term fault slip rates, distributed deformation rates, and forecast of seismicity in the western United States from joint fitting of community geologic, geodetic, and stress direction data sets. *Journal of Geophysical Research*, *114*(B11403). https://doi.org/10.1029/2009JB006317

Bomberger, C., Bendick, R., Flesch, L., & Ehlers, T. A. (2018). Spatial scales in topography and strain rate magnitude in the western United States. *Journal of Geophysical Research: Solid Earth*, *123*(7), 6086–6097. https://doi.org/10.1029/2018JB016135

DeMets, C., Gordon, R. G., & Argus, D. F. (2010). Geologically current plate motions. *Geophysical Journal International*, *181*, 1–80. https://doi.org/10.1111/j.1365-246x.2009.04491.x

El-Fiky, G. S., & Kato, T. (1998). Continuous distribution of the horizontal strain in the Tohoku district, Japan, predicted by least-squares collocation. *Journal of Geodynamics*, *27*(2), 213–236. https://doi.org/10.1016/S0264-3707(98)00006-4

Engwirda, D. (2014). *Locally-optimal Delaunay-refinement and optimisation-based mesh generation* (PhD Thesis). The University of Sydney, School of Mathematics and Statistics.

Feigl, K. L., Agnew, D. C., Bock, Y., Dong, D., Donnellan, A., Hager, B. H., et al. (1993). Space geodetic measurement of crustal deformation in central and southern California, 1984–1992. *Journal of Geophysical Research: Solid Earth*, *98*(B12), 21677–21712. https://doi.org/10.1029/93jb02405

Field, E. H., Arrowsmith, R. J., Biasi, G. P., Bird, P., Dawson, T. E., Felzer, K. R., et al. (2014). Uniform California earthquake rupture forecast version 3 (UCERF3): The time-independent model. *Bulletin of the Seismological Society of America*, *104*, 1122–1180. https://doi.org/10.1785/0120130164

Flesch, L. M., Holt, E. E., Silver, P. G., Stephenson, M., Wang, C.-Y., & Chan, W. W. (2005). Constraining the extent of crust-mantle coupling in central Asia using GPS, geologic, and shear wave splitting data. *Earth and Planetary Science Letters*, *238*(1–2), 248–268. https://doi.org/10.1016/j.epsl.2005.06.023

Flesch, L. M., Holt, W. E., Haines, A. J., Wen, L., & Shen-Tu, B. (2007). The dynamics of western North America: Stress magnitudes and the relative role of gravitational potential energy, plate interaction at the boundary and basal tractions. *Geophysical Journal International*, *169*(3), 866–896. https://doi.org/10.1111/j.1365-246X.2007.03274.x

Fukuda, J., & Johnson, K. M. (2010). Mixed linear—Non-linear inversion of crustal deformation data: Bayesian inference of model, weighting and regularization parameters. *Geophysical Journal International*, *181*(3), 1441–1458. https://doi.org/10.1111/j.1365-246x.2010.04564.x

Ghosh, A., Holt, W., & Wen, L. (2013). Predicting the lithospheric stress field and plate motions by joint modeling of lithosphere and mantle dynamics. *Journal of Geophysical Research*, *118*(1), 346–368. https://doi.org/10.1029/2012jb009516

Ghosh, A., & Holt, W. E. (2012). Plate motions and stresses from global dynamic models. *Science*, *335*(6070), 838–843. https://doi.org/10.1126/science.1214209

Goudarzi, M. A., Cocard, M., & Santerre, R. (2015). GeoStrain: An open source software for calculating crustal strain rates. *Computers & Geosciences*, *82*, 1–12. https://doi.org/10.1016/j.cageo.2015.05.007

Gray, H. J., Shobe, C. M., Hobley, D. E., Tucker, G. E., Duvall, A. R., Harbert, S. A., & Owen, L. A. (2017). Off-fault deformation rate along the southern San Andreas fault at Mecca Hills, southern California, inferred from landscape modeling of curved drainages. *Geology*, *46*(1), 59–62. https://doi.org/10.1130/G39820.1

Hackl, M., Malservisi, R., & Wdowinski, S. (2009). Strain rate patterns from dense GPS networks. *Natural Hazards and Earth System Sciences*, *9*(4), 1177–1187. https://doi.org/10.5194/nhess-9-1177-2009

Haines, A. J., Dimitrova, L. L., Wallace, L. M., & Williams, C. A. (2015). Introduction to the vertical derivatives of horizontal stress (VDoHS) rates. In A. J. Haines, L. L. Dimitrova, L. M. Wallace, & C. A. Williams (Eds.), *Enhanced surface imaging of crustal deformation: Obtaining tectonic force fields using GPS data. SpringerBriefs in Earth Sciences* (pp. 9–18). Springer International Publishing. https://doi.org/10.1007/978-3-319-21578-5_2

Haines, A. J., & Holt, W. E. (1993). A procedure to obtain the complete horizontal motions within zones of distributed deformation from the inversion of strain rate data. *Journal of Geophysical Research*, *98*, 12057–12082.

Hardebeck, J. L., & Hauksson, E. (2001). Crustal stress field in southern California and its implications for fault mechanics. *Journal of Geophysical Research*, *106*(B10), 21859–21882. https://doi.org/10.1029/2001jb000292

Hardebeck, J. L., & Okada, T. (2018). Temporal stress changes caused by earthquakes: A review. *Journal of Geophysical Research: Solid Earth*, *123*(2), 1350–1365. https://doi.org/10.1002/2017JB014617

Harris, R. A., & Segall, P. (1987). Detection of a locked zone at depth on the Parkfield, California, segment of the San Andreas fault. *Journal of Geophysical Research*, *92*(B8), 7945–7962. https://doi.org/10.1029/JB092iB08p07945

Hatem, A. E., Collett, C. M., Briggs, R., Gold, R. D., Angster, S. J., Powers, P. M., et al. (2022). Earthquake geology inputs for the US National Seismic Hazard Model (NSHM) 2023 (western US) (ver. 2.0, February 2022). https://doi.org/10.5066/P9AU713N

Heidbach, O., Rajabi, M., Reiter, K., & Ziegler, M. (2016). World Stress Map 2016. https://doi.org/10.5880/WSM.2016.002

Herbert, J. W., Cooke, M. L., Oskin, M., & Difo, O. (2013). How much can off-fault deformation contribute to the slip rate discrepancy within the eastern California shear zone? *Geology*, *42*(1), 71–75. https://doi.org/10.1130/g34738.1

Herbert, J. W., Cooke, M. L., Oskin, M., & Difo, O. (2014). How much can off-fault deformation contribute to the slip rate discrepancy within the eastern California shear zone? *Geology*, *42*(1), 71–75. https://doi.org/10.1130/G34738.1

Humphreys, E. D., & Coblentz, D. D. (2007). North American dynamics and western US tectonics. *Reviews of Geophysics*, *45*(3). https://doi.org/10.1029/2005RG000181

Johnson, K. (2023a). Johnson 2023 strain rate and velocity realizations for western US [Dataset]. https://doi.org/10.5281/zenodo.8140537

Johnson, K. M. (2023b). BforStrain [Software]. *Zenodo, v1.0.0*. https://doi.org/10.5281/zenodo.8029961

Kreemer, C., Blewitt, G., & Klein, E. C. (2014). A geodetic plate motion and global strain rate model. *Geochemistry, Geophysics, Geosystems*, *15*(10), 3849–3889. https://doi.org/10.1002/2014GC005407

Kreemer, C., Hammond, W. C., & Blewitt, G. (2018). A robust estimation of the 3-D intraplate deformation of the North American plate from GPS. *Journal of Geophysical Research: Solid Earth*, *123*(5), 4388–4412. https://doi.org/10.1029/2017JB015257

Kreemer, C., & Young, Z. M. (2022). Crustal strain rates in the western United States and their relationship with earthquake rates. *Seismological Research Letters*, *93*(6), 2990–3008. https://doi.org/10.1785/0220220153

Levandowski, W., Herrmann, R. B., Briggs, R., Boyd, O., & Gold, R. (2018). An updated stress map of the continental United States reveals heterogeneous intraplate stress. *Nature Geoscience*, *11*(6), 433–437. https://doi.org/10.1038/s41561-018-0120-x

Liu, S., Shen, Z.-K., Bürgmann, R., & Jónsson, S. (2020). Thin crème brûlée rheological structure for the Eastern California Shear Zone. *Geology*, *49*(2), 216–221. https://doi.org/10.1130/G47729.1

McCaffrey, R. (2005). Block kinematics of the Pacific-North America plate boundary in the southwestern United States from inversion of GPS, seismological, and geologic data. *Journal of Geophysical Research*, *110*(B07401). https://doi.org/10.1029/2004JB003307

Meade, B. J., Hager, B. H., & King, R. W. (2002). Block models of present day deformation in southern California constrained by geodetic measurements (abstract), 2002. SCEC Annual Meeting, Oxnard CA (p. 96).

Noda, A., & Matsu'ura, M. (2010). Physics-based GPS data inversion to estimate three-dimensional elastic and inelastic strain fields. *Geophysical Journal International*, *182*(2), 513–530. https://doi.org/10.1111/j.1365-246X.2010.04611.x

Pagani, C., Bodin, T., Métois, M., & Lasserre, C. (2021). Bayesian estimation of surface strain rates from global navigation satellite system measurements: Application to the southwestern United States. *Journal of Geophysical Research: Solid Earth*, *126*(6). https://doi.org/10.1029/2021JB021905

Petersen, M. D., Moschetti, M. P., Powers, P. M., Mueller, C. S., Haller, K. M., Frankel, A. D., et al. (2014). Documentation for the 2014 update of the United States national seismic hazard maps: U.S. Geological Survey Open-File Report 2014–1091. 243 p. https://doi.org/10.3133/ofr20141091

Pollitz, F. (2015). Post-earthquake relaxation evidence for laterally variable viscoelastic structure and water content in the southern California mantle. *Journal of Geophysical Research*, *120*(4), 2672–2696. https://doi.org/10.1002/2014JB011603

Pollitz, F. F., Evans, E. L., Field, E. H., Hatem, A. E., Hearn, E. H., Johnson, K., et al. (2022). Western US deformation models for the 2023 update to the US National Seismic Hazard Model. *Seismological Research Letters*, *93*(6), 3068–3086. https://doi.org/10.1785/0220220143

Pollitz, F. F., Wicks, C., & Thatcher, W. (2001). Mantle flow beneath a continental strike-slip fault: Postseismic deformation after the 1999 hector mine earthquake. *Science*, *293*(5536), 1814–1818. https://doi.org/10.1126/science.1061361

Sandwell, D. T., & Wessel, P. (2016). Interpolation of 2-D vector data using constraints from elasticity. *Geophysical Research Letters*, *43*(20), 10703–10709. https://doi.org/10.1002/2016GL070340

Savage, J. C. (1983). A dislocation model of strain accumulation and release at a subduction zone. *Journal of Geophysical Research*, *88*(B6), 4984–4996. https://doi.org/10.1029/jb088ib06p04984

Savage, J. C., & Burford, R. (1973). Geodetic determination of relative plate motion in central California. *Journal of Geophysical Research*, *78*(5), 832–845. https://doi.org/10.1029/jb078i005p00832

Savage, J. C., & Simpson, R. W. (1997). Surface strain accumulation and the seismic moment tensor. *Bulletin of the Seismological Society of America*, *87*(5), 1345–1353. https://doi.org/10.1785/bssa0870051345

Shen, Z., & Bird, P. (2022). NeoKinema deformation model for the 2023 update to the US National Seismic Hazard Model. *Seismological Research Letters*, *93*(6), 3037–3052. https://doi.org/10.1785/0220220179

Shen, Z., Wang, M., Zeng, Y., & Wang, F. (2015). Optimal interpolation of spatially discretized geodetic data. *Bulletin of the Seismological Society of America*, *105*(4), 2117–2127. https://doi.org/10.1785/0120140247

Shen, Z.-K., Jackson, D. D., & Ge, B. X. (1996). Crustal deformation across and beyond the Los Angeles basin from geodetic measurements. *Journal of Geophysical Research*, *101*(B12), 27957–27980. https://doi.org/10.1029/96jb02544

Tape, C., Musé, P., Simons, M., Dong, D., & Webb, F. (2009). Multiscale estimation of GPS velocity fields. *Geophysical Journal International*, *179*(2), 945–971. https://doi.org/10.1111/j.1365-246X.2009.04337.x

Townend, J., & Zoback, M. D. (2001). Implications of earthquake focal mechanisms for the frictional strength of the San Andreas fault system. In R. E. Holdsworth, R. A. Strachan, J. F. Magloughlin, & R. J. Knipe (Eds.), *Geological society, London, special publications, the nature and tectonic significance of fault zone weakening* (Vol. 186(1), pp. 13–21). The Geological Society of London. https://doi.org/10.1144/gsl.sp.2001.186.01.02

Townend, J., & Zoback, M. D. (2004). Regional tectonic stress near the San Andreas fault in central and southern California. *Geophysical Research Letters*, *31*(15). https://doi.org/10.1029/2003GL018918

Townend, J., & Zoback, M. D. (2006). Stress, strain, and mountain building in central Japan. *Journal of Geophysical Research*, *111*(B3). https://doi.org/10.1029/2005JB003759

Wang, K. (2000). Stress–strain 'paradox', plate coupling, and forearc seismicity at the Cascadia and Nankai subduction zones. *Tectonophysics*, *319*(4), 321–338. https://doi.org/10.1016/S0040-1951(99)00301-7

Ward, S. N. (1994). Constraints on the seismotectonics of the central mediterranean from very long baseline interferometry. *Geophysical Journal International*, *117*(2), 441–452. https://doi.org/10.1111/j.1365-246x.1994.tb03943.x

Ward, S. N. (1998). On the consistency of earthquake moment rates, geological fault data, and space geodetic strain: The United States. *Geophysical Journal International*, *134*(1), 172–186. https://doi.org/10.1046/j.1365-246x.1998.00556

Wessel, P., Smith, W. H. F., Scharroo, R., Luis, J., & Wobbe, F. (2013). Generic mapping tools: Improved version released. *Eos, Transactions American Geophysical Union*, *94*(45), 409–410. https://doi.org/10.1002/2013EO450001

Yang, Y.-R., Johnson, K. M., & Chuang, R. Y. (2013). Inversion for absolute deviatoric crustal stress using focal mechanisms and coseismic stress changes: The 2011 M9 Tohoku-oki, Japan, earthquake. *Journal of Geophysical Research*, *118*(10), 5516–5529. https://doi.org/10.1002/jgrb.50389

Zeng, Y. (2022). GPS velocity field of the western United States for the 2023 National Seismic Hazard Model Update. *Seismological Research Letters*, *93*(6), 3121–3134. https://doi.org/10.1785/0220220180

Zeng, Y., Petersen, M. D., & Shen, Z.-K. (2018). Earthquake potential in California-Nevada implied by correlation of strain rate and seismicity. *Geophysical Research Letters*, *45*(4), 1778–1785. https://doi.org/10.1002/2017GL075967